JGR Solid Earth

RESEARCH ARTICLE
10.1029/2024JB029138

Xenolith Petrochronology (San Luis Potosi, Mexico) Constrains Heat Sources for Cenozoic Ultrahigh-Temperature Metamorphism in the Lower Crust

Omar Khalil Droubi[1,2], **Jacob H. Cipar**[1], **Andrew J. Smye**[1], **and Joshua M. Garber**[1]

[1]Department of Geosciences, The Pennsylvania State University, University Park, PA, USA, [2]Now at Department of Geoscience, University of Wisconsin-Madison, Madison, WI, USA

Key Points:

- Lower crustal metapelite xenoliths from San Luis Potosi, Mexico record ultrahigh (>900°C) temperature (UHT) metamorphism
- Zircon petrochronology suggests protracted (>15 Myr) UHT conditions since the onset of regional extension
- Garnet preserves complex trace-element zoning despite extreme temperatures; garnet diffusion chronometry timescales agree with zircon data

Correspondence to:
O. K. Droubi,
droubi@wisc.edu

Citation:
Droubi, O. K., Cipar, J. H., Smye, A. J., & Garber, J. M. (2024). Xenolith petrochronology (San Luis Potosi, Mexico) constrains heat sources for Cenozoic ultrahigh-temperature metamorphism in the lower crust. *Journal of Geophysical Research: Solid Earth*, *129*, e2024JB029138. https://doi.org/10.1029/2024JB029138

Received 20 MAR 2024
Accepted 21 JUL 2024

Author Contributions:
Conceptualization: Jacob H. Cipar, Andrew J. Smye
Data curation: Omar Khalil Droubi, Jacob H. Cipar
Formal analysis: Omar Khalil Droubi, Jacob H. Cipar, Andrew J. Smye
Funding acquisition: Andrew J. Smye
Investigation: Omar Khalil Droubi, Jacob H. Cipar, Joshua M. Garber
Methodology: Omar Khalil Droubi, Jacob H. Cipar, Andrew J. Smye, Joshua M. Garber
Project administration: Andrew J. Smye
Resources: Andrew J. Smye, Joshua M. Garber
Software: Omar Khalil Droubi, Jacob H. Cipar, Andrew J. Smye
Supervision: Andrew J. Smye, Joshua M. Garber

Abstract Ultrahigh-temperature (UHT; >900°C) metamorphism drives crustal differentiation and is widely recognized in the rock record, but its geodynamic causes are debated. Previous work on granulite-facies metapelite xenoliths from San Luis Potosí, Mexico suggests the lower crust experienced a protracted UHT metamorphic event that coincided with the onset of regional extension. To determine the duration, conditions, and heat sources of UHT metamorphism recorded by these xenoliths, this study characterizes the major-element, trace-element, and U-Pb isotopic systematics of quartz, rutile, feldspar, garnet, and zircon by in situ electron microprobe (EPMA) and laser-ablation inductively coupled-plasma mass spectrometry (LA-ICP-MS), and augments these data with detailed petrography, thermobarometry, phase equilibria modeling, and diffusion modeling. Thermobarometry and phase equilibria modeling suggest peak metamorphic conditions exceeded 0.7 GPa and 900°C. Zircon petrochronology confirms >15 Myr of UHT conditions since its onset at ∼30 Ma. A small population of zircon record elevated temperatures following transition from backarc compression to extension during the waning stages of orogenesis (60–37 Ma). Garnet preserves trace-element zoning and mineral inclusions consistent with suprasolidus garnet growth and subsequent compositional modification by intracrystalline rare-earth element diffusion during protracted heating, with diffusion chronometry timescales in agreement with zircon data, followed by fluid-driven remobilization of trace elements along now-healed fractures within ∼1 Myr of eruption. In sum, these data are most compatible with lithospheric mantle attenuation or removal as the dominant heat transport mechanism driving synextensional UHT metamorphism and crustal melting, which has bearing on models for crustal differentiation and formation of modern and ancient granulite terranes globally.

Plain Language Summary The production of melt in the deep crust has important implications for how continents are physically and chemically modified, which in turn controls the distribution of critical mineral resources and the expression of plate tectonics at Earth's surface. One setting where significant partial melting can occur is in a high-temperature granulite terrane, such as the lower crust beneath the Basin and Range province of southwestern North America. The Basin and Range province is a region where the continent is actively experiencing tectonic extension and, in several places, has been interpreted to have lower crust that was (or is currently) heated to above 900°C. To understand the causality between continental extension in North America and these extreme metamorphic conditions, we study exotic rock fragments of the deep crust beneath San Luis Potosí, Mexico that were brought up by a geologically recent volcanic eruption. These rocks record chemical information that tracks the temperature of the geologically modern lower crust prior to eruption and the duration of extreme temperatures and melting in this crust over the last 60 million years. Using this chemical information, we further our understanding of how tectonic extension is actively driving deep crustal melting beneath southwestern North America.

1. Introduction

Within the continental crust, the addition or dissipation of heat is one of the primary controls on metamorphic assemblage, rheology, and anatexis. The addition of heat can rheologically weaken and/or melt the crust, especially the lower crust, where lower crustal flow and melt transport to shallower depths are the dominant forms of mechanical (Arzi, 1978; Hyndman, 2017) and chemical differentiation (e.g., Bown & White, 1995; Brown, 2013; Clemens, 1990; Herzberg et al., 1983; Sawyer et al., 2011; Vielzeuf et al., 1990). Further, global data sets of continental lower crust, constructed through study of deeply exhumed, granulite-facies terranes and

Validation: Omar Khalil Droubi, Jacob H. Cipar, Joshua M. Garber
Visualization: Omar Khalil Droubi
Writing – original draft: Omar Khalil Droubi, Jacob H. Cipar
Writing – review & editing: Omar Khalil Droubi, Andrew J. Smye, Joshua M. Garber

lower crustal xenoliths, demonstrate that the lower crust commonly contains both mafic and felsic (peraluminous) components (Dumond et al., 2018; Hacker et al., 2015; Rudnick & Gao, 2003; Sammon & McDonough, 2021). These peraluminous lithologies have higher concentrations of heat-producing elements (K, Th, U), as well as higher silica content due to increased amounts of quartz, resulting in relatively weaker rheology (Bürgmann & Dresen, 2008), higher rates of radiogenic heat production, and–at anhydrous conditions–lower temperature initiation of melt generation (Vielzeuf & Holloway, 1988).

This study focuses on a lower-crustal section with well-documented evidence for pervasive suprasolidus conditions: the modern metapelitic lower crust beneath the Mexican Basin and Range (Hayob et al., 1989; Figure 1). Previous work on metapelite xenoliths suggests that the lower crust beneath the Quaternary cinder cone Cerro El Toro (San Luis Potosi, Mexico) experienced prolonged UHT conditions from ∼27 to 6 Ma (Hayob et al., 1989; Solari et al., 2023), with the timing of metamorphism correlative to the timing of regional extension (Henry & Aranda-Gomez, 1992; Sedlock et al., 1993), similar to interpretations made for the lower crust beneath Kilbourne Hole maar, New Mexico, USA (Cipar et al., 2020). It is well-documented that felsic rocks subjected to UHT metamorphic conditions at crustal pressures undergo large magnitudes of partial melt production and extraction (e.g., Brown, 2013; Clemens, 2006; Harley, 1989; Hokada & Harley, 2004; Jiao et al., 2023), however the tectonic affinity, thermal drivers, and timescales of UHT–and thus anatexis–at these conditions remain incompletely understood.

To explain synextensional, lower crustal UHT in Mexico, possible heating mechanisms include (a) focused radiogenic heating during orogenic collapse (Jamieson et al., 2004); (b) viscous dissipation, or shear heating, during ductile deformation of the lithosphere (e.g., Nabelek et al., 2010; Whittington et al., 2009); (c) continuous conductive heat transfer from upwelling asthenosphere (Platt & England, 1994) in response to convective removal or thinning of mantle lithosphere (e.g., Bird, 1979; Sandiford & Powell, 1990); (d) advective heat delivered by intrusion of mafic magmas (e.g., Annen & Sparks, 2002); or (e) a combination of the above. Discriminating between these competing geodynamic mechanism requires robust pressure-temperature-time (P-T-t) paths determined from rock-forming mineral phases, yet such path-related information cannot typically be extracted from minerals that experience UHT conditions due to the exponential dependence of elemental diffusivities on temperature (e.g., Caddick et al., 2010; Frost & Chacko, 1989), which flattens or erases most prograde chemical information during even short residence times at UHT. However, trace elements (TE) within phases such as rutile (Cherniak, Manchester, & Watson, 2007), quartz (Audétat et al., 2021, 2023; Cherniak, Watson, Wark, 2007; Jollands et al., 2020), zircon (Bloch et al., 2022; Cherniak, 2010; Cherniak & Watson, 2007), and garnet (Bloch et al., 2015, 2020) are more robust to diffusional re-equilibration at high temperature making them valuable targets for interrogating prograde metamorphic histories. Here, we characterize the major-element, TE, and U-Pb isotopic systematics of feldspar, quartz, rutile, zircon, and garnet within lower crustal metapelite xenoliths from Cerro El Toro (Figure 1) using electron beam microscopy and LA-ICP-MS, and combine these data with detailed petrography, thermobarometry, phase equilibria modeling, and diffusion modeling, providing a host of new constraints on the timing, duration, and mechanisms of UHT metamorphism in the lower crust of north-central Mexico.

2. Geologic Background

The xenoliths in this study are hosted in alkaline basalts of the Cerro El Toro cinder cone (22° 50.97′ N, 101° 29.81′ W, WGS84; San Luis Potosí, Mexico), located within the Ventura-Espíritu Santo Volcanic Field in the southern portion of the Mesa Central (Figure 1). The Mesa Central is a high elevation (>1,800 m above sea level) plateau (Raisz, 1964) with an estimated crustal thickness varying between ∼30 and 45 km (e.g., Nieto-Samaniego et al., 2007; Peredo et al., 2021). The Mesozoic-Cenozoic evolution of north-central Mexico and the Mesa Central remains an active field of study and, like the western USA, tectonic models remain contentious amongst different researchers (i.e., Martini & Ortega-Gutiérrez, 2018). However, it is broadly agreed upon that the geologic evolution of north-central Mexico is dominated by a complex cycle of basin formation, deformation, and magmatism attributed to alternating intervals of roughly NE-SW supra-subduction rifting and contraction related to subduction zone evolution to the west and south of our field area, along the Pacific margin of North American plate (i.e., Fitz-Díaz et al., 2018; Martini & Ortega-Gutiérrez, 2018).

From the Late Triassic to the Middle Jurassic, eastward subduction drove erosion of the Permo-Triassic continental arc and deposition of submarine fans along the Pacific margin of Mexico (Barboza-Gudiño et al., 2010;

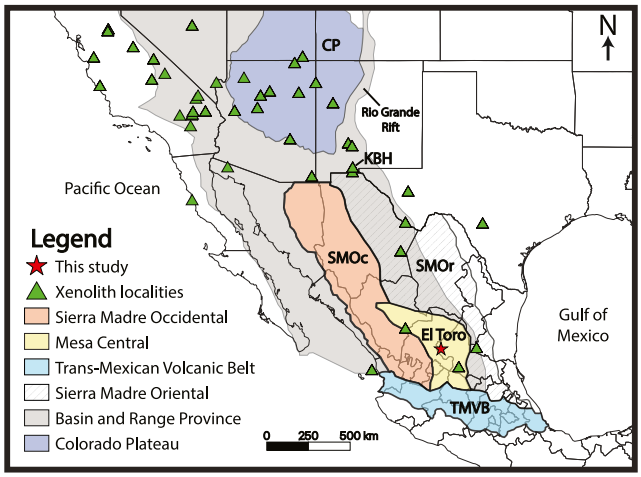

Figure 1. Simplified geologic map of Mexico and southwestern US, showing state boundaries and xenolith localities, including locality of our samples, as well as significant geologic provinces. Xenolith localities are from Wilshire et al. (1988); Rudnick and Cameron (1991); Housh et al. (2010); Raye et al. (2011); Cameron and Ward (1998); Stull and McMillan (1973); Pool (1990); Warren et al. (1979); Aranda-Gomez et al. (1992); Aranda-Gomez et al. (2010); and Luhr et al. (1989). Geologic province positions and extents are modified from Tristán-González et al. (2009); Dickinson (2006); and Aguirre-Díaz et al. (2008).

Silva-Romo et al., 2000). Slab rollback of the Farallon plate began in the Middle Jurassic, initiating rifting of the Gulf of Mexico, widespread Jurassic magmatism west of the present-day Mesa Central, and development of several basins–including the Arperos back-arc basin and Central Mexico basin (Fitz-Díaz et al., 2018; Martini & Ortega-Gutiérrez, 2018). Subsequently, the Sierra Madre Oriental fold-and-thrust belt, exposed to the north and east of our study area (Figure 1), formed in response to the Mexican orogeny (Fitz-Díaz et al., 2018), which was coeval with the Sevier and Laramide orogenies further to the north (English & Johnston, 2004). Compressional deformation from the Mexican orogeny is attributed to the closure of the Arperos basin during accretion of the Guerrero terrane to continental Mexico (~118–112 Ma; Martini & Ortega-Gutiérrez, 2018; Martini et al., 2009) followed by shallowing eastward subduction of the Farallon plate that resulted in formation of the Tarahumara continental arc (105-80 Ma; i.e., Centeno-García, 2017) along the Pacific margin of Mexico. Sporadic inland magmatism occurred until about ~55 Ma (Ferrari et al., 2018; Nieto-Samaniego et al., 2007), when the presence of undeformed igneous rocks signifies a transition away from a compressive stress field in the Mesa Central. At this time, the gently dipping Farallon slab once again began to rollback and the Mesa Central transitioned to back-arc extension with associated magmatism (~54–38 Ma) (Ferrari et al., 2018). Around ~35 Ma, there was a rapid slowing of relative convergence between the Farallon and North American plates, which continued until Farallon subduction terminated at ~13–12 Ma (Ferrari et al., 2018). While the Farallon plate slowed and rolled back, parts of the underlying slab may have detached and foundered (~36–30 Ma), including beneath the Mesa Central (Ferrari et al., 2018). This timing coincides with the ~30–24 Ma development of a regional E-W extensional stress field and normal faulting associated with Basin and Range extension (Henry & Aranda-Gomez, 1992; Sedlock et al., 1993), elevated surface heat flow (>70 mW m^{-2}; Blackwell & Richards, 2004; Blackwell et al., 2011), and large-volume silicic magmatism (initial pulse from ~34 to 28 Ma and second pulse from ~24 to 18 Ma; Ferrari et al., 2018) that comprises the bulk of the Sierra Madre Occidental (McDowell et al., 1979) directly west of the Mesa Central (Figure 1). Pulses of extensional normal-faulting near Cerro El Toro are dated at ~31–29 Ma and <16.5 Ma (Aranda-Gómez et al., 2007; Del Pilar-Martínez et al., 2021). South of the Mesa Central lies the Trans-Mexican Volcanic Belt (Figure 1), a continental arc, with magmatism beginning at its east side around ~20 Ma, associated with ongoing subduction of the Rivera microplate and the northern part of the Cocos plate (Ferrari et al., 2012).

Intraplate-type alkalic volcanism in the Mesa Central is grouped into the Los Encinos Volcanic Field (13.6–10.6 Ma; Luhr et al., 1995) and the Santo Domingo and Ventura-Espiritu Santo Volcanic Fields (~6–0.4 Ma; Aranda-Gómez & Luhr, 1996; Solari et al., 2023). Common eruptive products of the Ventura-Espiritu Santo Volcanic Field include xenolith-bearing olivine-nephelinite and basanite, with peridotite, pyroxenite, two-pyroxene granulite, charnockite, and garnet-bearing metapelite xenoliths, the latter of which have been the focus of significant study (e.g., Hayob et al., 1989; Luhr & Aranda-Gómez, 1997; Luhr et al., 1989; Pool, 1990; Ruiz et al., 1988; Schaaf et al., 1994). Early research on the metapelite xenoliths from Cerro El Toro derived equilibrium P-T estimates of 0.9–1.3 GPa and >870°C, based on two-feldspar thermometry and garnet-aluminosilicate-plagioclase-silica (GASP) barometry (Hayob et al., 1989, 1990). Researchers speculated that the granulite-facies metamorphism occurred by Tertiary basaltic underplating, but these studies lacked definitive geochronologic data to test this hypothesis (Harley, 1990; Harte & Barnicoat, 1990). In addition to sampling the xenoliths used by this study, Pool (1990) analyzed bulk rock major- and TE compositions from a subset of metapelite xenoliths from Cerro El Toro, which were consistent with LILE-depleted shale protoliths and comparable to pelitic paragneiss xenoliths at Kilbourne Hole, USA (Reid et al., 1989). Recent work by Solari et al. (2023) compared the breached cone morphology of Cerro El Toro to better-studied volcanic fields with similar climatic conditions (e.g., Camargo Volcanic Field: Aranda-Gómez et al., 2003) and suggested the volcano must be <6 Ma in age. Solari et al. (2023) used LA-split stream (SS)-ICP-MS to analyze zircon from the metapelite xenoliths of El Toro and found that the zircon U-Pb dates ranged from ~5 to 1,183 Ma, with subpopulations of zircon classified as igneous or metamorphic based on chondrite-normalized HREE slope. By

comparing ages and TE of inherited igneous zircon cores from the Cerro El Toro metapelite xenoliths with detrital zircons from modern Mexican Pacific coast sediments, Solari et al. (2023) hypothesized that the zircon grains within the xenoliths were originally contained in sediments with mid-Eocene-Oligocene depositional ages. These sediments were posited to have been subducted with the Farallon plate and transported diapirically to the base of the crust, before experiencing a protracted UHT metamorphic event spanning ∼27 Ma to ∼6 Ma (Solari et al., 2023). While determining the mechanism by which these sediments were "relaminated"–i.e., transported from the surface to the base of the crust–is important, our study focuses on the history of these sediments after their relamination, and the term "relamination" is used in this manuscript to describe the transport of sediments from surface to base of the crust without ascribing a tectonic mechanism.

3. Methods

3.1. SEM and EPMA

To identify/map major elements within the major rock-forming phases of the studied xenoliths, as well as characterize textures and inclusions, energy dispersive X-ray spectroscopy (EDS) and back-scattered electron imaging were employed with CAMECA SXFive Electron Probe Microanalyzers (EPMA) at the Material Research Institute at Penn State and at Syracuse University. Quantitative wavelength dispersive spectroscopy (WDS) measurements of major-element concentrations within garnet and feldspar were conducted in thin sections using the following operating conditions: beam current set to 30 nA (Penn State)/10 nA (Syracuse), accelerating voltage at 15 kV, take-off angle at 40°, and the beam diameter <1 μm ("focused beam"). A range of natural and synthetic reference materials were employed to optimize matrix-matching between reference material and analyte mineral phase, with specific attention paid to using reference materials with similar solid solution compositions (i.e., almandine garnet) to analyte mineral phases. In addition to analyzing major elements in garnet and feldspar, Ti and Zr were measured in quartz and rutile in thin sections, respectively, at Syracuse University using the Cameca SXFive EPMA, following the methods in Osborne et al. (2022). To avoid secondary fluorescence effects, measurements on quartz were performed >50 μm from rutile and measurements on rutile were performed >50 μm from zircon. To avoid inclusions/outliers, only EPMA data that met the following constraints was used: for garnet: total oxides >98 wt. %, 16.6 wt.% < Si < 20.4 wt.%, 10 wt.% < Al < 14 wt.%; for feldspar: total oxides >97%, Si < 24 wt.%; and for quartz/rutile: total oxides >95 wt. %. Prior to LASS-ICP-MS analysis, zircon cathodoluminescence (CL) images (accelerating voltage of 15 keV) were obtained on polished grain surfaces using a Zeiss Sigma variable pressure field emission scanning electron microscope (VP-FE-SEM) at the Material Research Institute at Penn State.

3.2. LA-ICP-MS Garnet

LA-ICP-MS trace-element spot transects across garnet within thin sections from five different samples were performed at the Penn State LionChron facility, followed by garnet grid-mapping sessions for specific garnets in thin sections from samples SLP200E and SLP200H, as well as a garnet in lower crustal metapelite Kilbourne Hole xenolith DEKH2 (Droubi et al., 2024). Measurements were made using a Teledyne/Photon Machines Analyte G2 193 nm Excimer laser ablation system, coupled to a Thermo Scientific iCAP RQ-ICP-MS. Sample gas flows were tuned to maximize sensitivity prior to analysis, with 0.44 L/min total He and 1.00 L/min total Ar. Operating conditions for spot analyses consisted of 20 μm squares, fluence = 3.045 J cm^{-2}, 150 shots at 10 Hz repetition rates (15 s of ablation), with 3 pre-ablation shots, and a total cycle time of ∼485 ms. Operating conditions for mapping consisted of 20 μm squares, fluence = 4.47 J cm^{-2}, 90 shots at 15 Hz repetition rates (6 s of ablation), with 3 pre-ablation shots, and a total cycle time of ∼425–446 ms. Trace elements were measured at the following masses: ^{27}Al (also used as the internal standard), ^{29}Si, ^{31}P, ^{43}Ca, ^{45}Sc, ^{49}Ti, ^{51}V, ^{52}Cr, ^{55}Mn, ^{89}Y, ^{90}Zr, ^{146}Nd, ^{147}Sm, ^{153}Eu, ^{157}Gd, ^{159}Tb, ^{163}Dy, ^{165}Ho, ^{166}Er, ^{169}Tm, ^{172}Yb, ^{175}Lu, $^{178/180}$Hf, and ^{238}U; ^{24}Mg, ^{57}Fe, ^{59}Co, ^{63}Cu, ^{66}Zn, ^{93}Nb, ^{139}La, ^{140}Ce, ^{141}Pr, and ^{208}Pb were measured in a subset of these runs (integration time per element = 3–30 ms).

Garnet trace-element data were reduced using Iolite v4.7 (Paton et al., 2011) and the "Trace Elements" data reduction scheme (Longerich et al., 1996), with the natural basaltic glass standard KL2G (GeoReM; Jochum et al., 2006) used as the primary bracketing standard. The use of glass standards for garnet trace-element measurements is common practice (e.g., Konrad-Schmolke et al., 2022; Rubatto et al., 2020), particularly given the absence of homogeneous natural garnet trace-element standards. Aluminum was used as the internal standard

element for trace element normalization, using average EPMA measured Al concentrations for garnets from each sample (11.7–12.2 wt. %) and published Al concentrations for all secondary standards. Outliers and inclusions were removed from the spot transect and map LA-ICP-MS data sets using petrographic context, as well as elemental cutoffs. Secondary glass standards SRM NIST 612, SRM NIST 614 (Pearce et al., 1997), ML3B, T1G, STHS6-80G, and ATHO-G (Georem, Jochum et al., 2006) were also analyzed in the same sessions. Secondary glass standard results indicate that–all measured TE of interest are within 10% of expected concentration, which is within the expected range of accuracy for LA-ICP-MS trace element measurements of glasses (Liu et al., 2008). Because Si drift on the iCAP behaves differently than other measured elements over the long duration (>12 hr) map analyses, Si concentration data for the maps is treated as "semi-quantitative."

3.3. LA-ICP-MS Zircon

Over three hundred spot analyses of specific CL domains in 64 polished zircon grains mounted in epoxy from six different xenolith samples were carried out by LASS-ICP-MS within the Penn State LionChron Facility over multiple sessions to measure trace-element and U-Th-Pb isotopic concentrations. Measurements were made using a Teledyne/Photon Machines Analyte G2 193 nm Excimer laser ablation system coupled to a Thermo Scientific Element XR HR-ICP-MS (U-Th-Pb isotopes) and a Thermo Scientific iCAP RQ-ICP-MS (TE), following the analytical configuration and Element XR analog correction factor (ACF) calibration method of Droubi et al. (2023). Operating conditions were 20 μm circular spot diameter, fluence = 3.05 J cm^{-2}, 200 shots at 10 Hz repetition rates (20 s of ablation), three cleaning shots with 15 s of washout between cleaning shots and analysis, and total cycle times <325 ms for both mass spectrometers. Using the Thermo Scientific iCAP, TE in zircon were measured at the following masses: ^{27}Al, ^{29}Si, ^{31}P, ^{45}Sc, ^{49}Ti, ^{89}Y, ^{93}Nb, ^{140}Ce, ^{141}Pr, ^{146}Nd, ^{147}Sm, ^{153}Eu, ^{157}Gd, ^{159}Tb, ^{163}Dy, ^{165}Ho, ^{166}Er, ^{169}Tm, ^{172}Yb, ^{175}Lu, ^{180}Hf (integration time per element = 5–50 ms; Ti specifically measured with 50 ms integration time). On the Element XR, U-Th-Pb isotopes of zircon were measured at the following masses: ^{204}Pb, ^{206}Pb, ^{207}Pb, ^{208}Pb, ^{232}Th, ^{235}U, ^{238}U (integration time per isotope = 1–131 ms). This split-stream configuration allows for high-precision U-Th-Pb isotopic measurements while contemporaneously measuring trace-element data from the same analyte volume without incorporating multiple ∼150 ms magnet jumps on the Element XR, which is especially critical for phases that potentially have small-scale chemical and isotopic heterogeneity, as described for the zircons in this study. Because this spatial and analytical trade-off limits the sensitivity of our LREE measurements in zircon, our interpretations are limited to the effect of HREE-bearing phases (i.e., garnet) co-crystallizing with zircon. After the ACF correction, the LASS-ICP-MS data were processed using the Iolite data reduction software v4.0 (Paton et al., 2011) with U-Th-Pb isotopes reduced using the "U-Pb Chronology" data reduction scheme (Paton et al., 2010) with a down-hole fractionation correction fit to a smoothed cubic spline with smoothing factor (A) = 0.995 and trace-elements reduced using the "Trace Elements" data reduction scheme (Longerich et al., 1996). Primary reference materials used include zircon 91500 (1,062.4 ± 0.4 Ma ID-TIMS ^{206}Pb/^{238}U date; Wiedenbeck et al., 2004) for U-Pb normalization and glass NIST SRM 612 (Pearce et al., 1997), with an assumed 15 wt.% Si in zircon, for trace-element normalization, while secondary zircon reference materials were GJ-1 (601.7 ± 1.3 Ma ID-TIMS ^{206}Pb/^{238}U date, Jackson et al., 2004), Plešovice (337.13 ± 0.37 Ma ID-TIMS ^{206}Pb/^{238}U date, Sláma et al., 2008), and Piexe (564 ± 4 Ma ID-TIMS ^{206}Pb/^{238}U date, Dickinson & Gehrels, 2003). Secondary zircon reference material U-Pb ages were within 2% of the accepted U-Pb ages across all analytical sessions. GJ-1 is the only zircon secondary reference material that is sufficiently homogeneous (Piazolo et al., 2017) to assess the accuracy of our trace-element routine; our approach yielded Ti, Y, M-HREE (Sm-Lu), and Hf concentrations within 10% of their published values. Stacey-Kramers-based ^{207}Pb/^{206}Pb age corrections (Stacey & Kramers, 1975) and Wetherill plotting are done using IsoplotR (Vermeesch, 2018), which uses the following constants: ^{238}U/^{235}U = 137.818 ± 0.0225 (Hiess et al., 2012), ^{238}U decay constant = 1.55×10^{-9} (y^{-1}), and ^{235}U decay constant = 9.849×10^{-9} (y^{-1}) (Jaffey et al., 1971).

4. Results

4.1. Samples

Five xenoliths from Cerro El Toro were chosen for detailed study based on modal distribution of metamorphic phases, the presence of zircon, and the preservation of garnet: SLP200E, SLP200C, SLP200F, SLP200H, and SLP200D. Zircon grains (100–200 μm) were separated from these five samples, as well as an additional sample (SLP200B), and mounted in epoxy rounds. Each sample except SLP200D shares the same broad mineralogy,

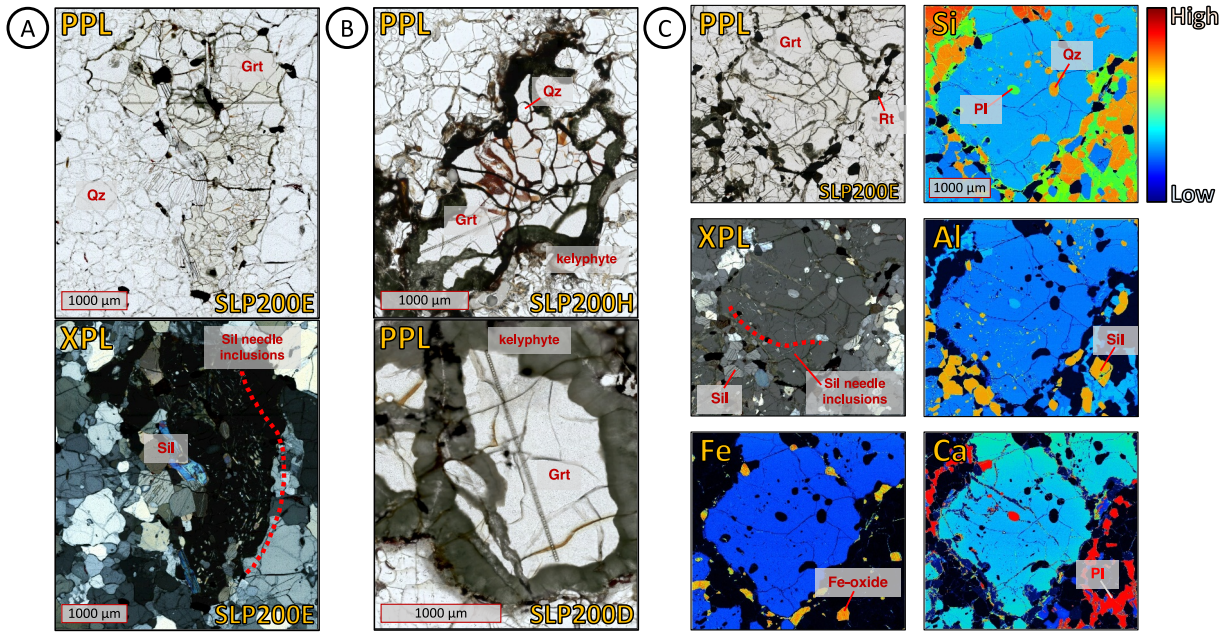

Figure 2. Photomicrographs of garnet-sillimanite xenoliths showing (a) pristine garnet, (b) the most kelyphytized samples, including the garnet mapped for SLP200H, and (c) the mapped garnet from SLP200E, with EDS X-ray maps discriminating between mineral phases.

consisting of garnet (0.2–5 mm diameter) + prismatic sillimanite (0.1–1.5 mm) + quartz (0.05–2.5 mm) + mesoperthitic feldspar (0.1–3 mm; <10 µm plagioclase bands exsolving along K-feldspar cleavage) + rutile (0.1–0.5 mm) often with thin (<20 µm) ilmenite rims + Fe-oxide (0.05–0.5 mm) + accessory ilmenite (0.05–0.5 mm) + accessory zircon (0.05–0.2 mm). Within all samples, garnet crystals are anhedral with embayed, lobate rims and have sub-domains with inclusions of rounded quartz, plagioclase, rutile, K-feldspar, zircon, and sillimanite. Most inclusions occur at random orientations in garnet crystals, except for sillimanite which forms as plates and needle-like inclusions that define a sigmoidal internal fabric within some garnet domains (Figure 2). Sillimanite inclusion fabrics are not observably consistent across different garnet crystals within the same sample. Notable differences between samples include: (a) SLP200E, SLP200C, and SLP200D display a weak foliation, defined by compositional layering and a shape preferred orientation of granoblastic quartz, feldspar, and sillimanite; (b) the best preserved garnet cores are in SLP200E, SLP200C, SLP200F (Figure 2a), whereas the largest garnet-melt/kelyphytization reaction rims and correspondingly fewer preserved garnet cores are in SLP200H, SLP200B, and SLP200D (Figure 2b); (c) SLP200D contains only a single ternary feldspar phase with no observable exsolution and very little sillimanite; (d) rare anhedral biotite (0.2–0.3 mm) grains are observed along grain boundaries in SLP200E and SLP200H; and (e) in contrast to the brown rutile in all other samples, SLP200F contains some rutile grains that are dark-blue (plane polarized light), a rutile color also observed in metapelite lower crustal Kilbourne Hole xenoliths (Ringwood et al., 2023).

4.2. Mineral Compositions

Major-element, TE, and U-Pb isotopic systematics of feldspar, quartz, rutile, zircon, and garnet were measured to determine inter- and intragrain mineral compositional variation and apply thermobarometry (see Discussion) for the studied xenoliths. EPMA WDS major- and TE data for quartz, feldspar, rutile, and garnet, LA-ICP-MS spot transect and grid map TE data for garnet, and LASS-ICP-MS TE and U-Pb isotopic data for zircon are reported in Supporting Information II in Droubi et al. (2024). In the metapelites with mesoperthitic feldspar, host K-feldspar has a composition of $Ab_{21–33}An_{3.4–5.3}Or_{62–75}$ with µm-scale plagioclase exsolution bands composed of $Ab_{51–55}An_{36–40}Or_{7.9–11}$ (Droubi et al., 2024). The non-exsolved ternary feldspar in SLP200D is $Ab_{61}An_{29}Or_{10}$ (Droubi et al., 2024). For four analyzed samples (SLP200E, SLP200C, SLP200H, SLP200D), measured Zr-in-rutile concentrations range from 1,650 to 6,970 ppm, and measured Ti-in-quartz ranges from 265 to 800 ppm. There are significant variations in Zr concentration

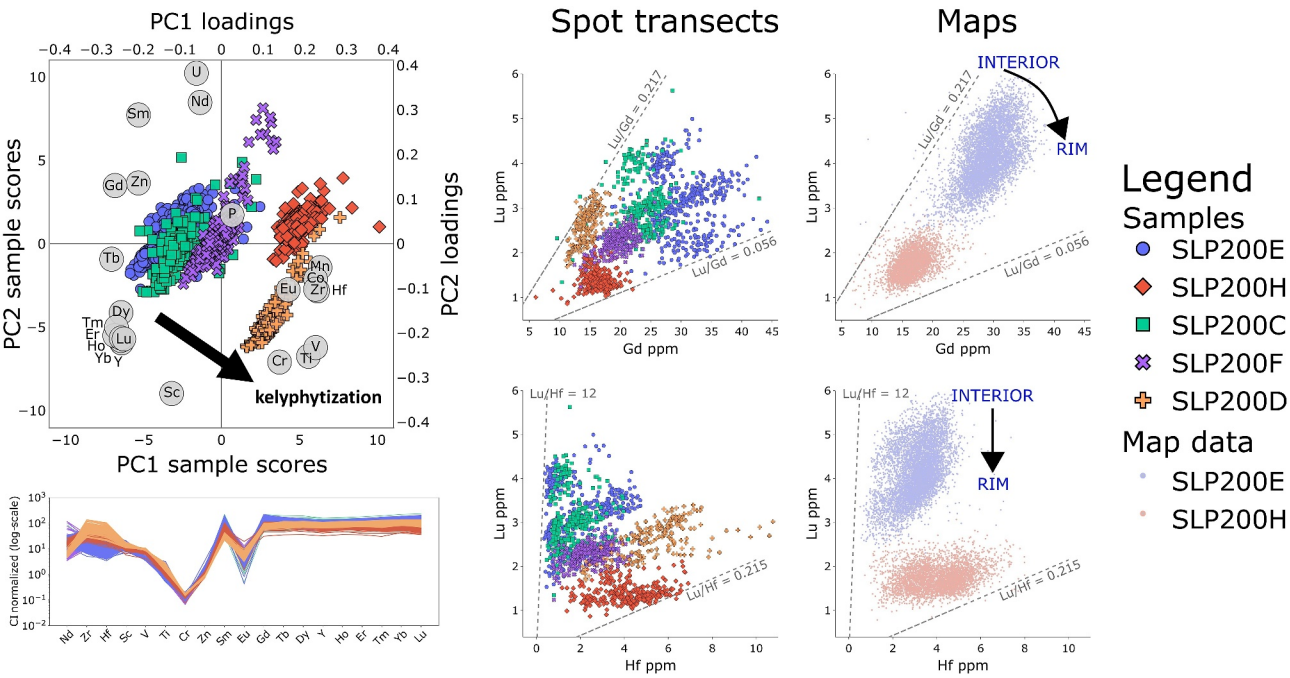

Figure 3. (Left) PCA biplot and trace-element spider diagram for garnet spot transect data set, colored and symboled by sample. (Center, right) Plots of Lu versus Gd concentration and Lu versus Hf concentration for garnet spot transect data set and garnet map data set.

among individual rutile grains at the thin section scale (e.g., 2,300–6,200 ppm in SLP200E). All garnets are almandine- and pyrope-rich ($Alm_{44–54}Prp_{41–52}Grs_{3.4–4.5}Sps_{0.8–1.5}$) (Droubi et al., 2024).

Trace-element data from twenty-seven in situ LA-ICP-MS spot transects–performed on five to six garnets per sample–demonstrate that all garnets have relatively flat chondrite-normalized rare-earth element (REE) patterns and negative Eu anomalies (Figure 3). Further interrogation by principal component analysis (PCA; see Droubi et al., 2024) reveals that *inter-sample* garnet TE variations are controlled by relative differences in concentrations of middle-to-heavy REE relative to high-field strength elements (HFSE) and transition metals (Figure 3). Further, garnet crystals from samples with observably higher degrees of kelyphytization, such as SLP200D and SLP200H (Figure 2), have less negative Eu anomalies and elevated concentrations of Mn, Ti, V, Cr, Co, Sc, Zr, and Hf relative to REE, Zn, and U (Figure 3). Phosphorus shows very little variation within the spot transect data set (Figure 3). There exists significant variation *within* individual samples, with garnet crystals from the same sample varying in HREE + Y versus MREE ratios, as well as REE concentrations relative to HFSE and transition metals (Figure 3). Notably, garnet grains from all five samples have variably elevated concentrations of Zr (≤500 ppm) and Hf (≤10 ppm), but all garnet has a constant, suprachondritic Zr/Hf ~50 (Droubi et al., 2024), which is broadly similar to the Zr/Hf ratios observed in garnet from Kilbourne Hole xenoliths (Ringwood et al., 2023). The compositions of the two mapped garnet grains (discussed further below) show wider intracrystalline variation but good overlap with the spot transect data (Figure 3), indicating that the mapped garnets are representative of the compositional breadth of garnet from the El Toro xenoliths.

Zircon exhibits significant U-Pb date dispersion, spanning 8.1 Ma to 1,183 Ma (Figure 4), and sample-scale and single grain TE chemical variability. Though there exist several discrete populations of concordant zircon domains, many analyses show varying degrees of discordance in Wetherill space (Figure 4; Wetherill, 1956), with no evidence for inclusion-related contamination based on TE compositions. To account for this observed discordance, if a zircon analysis has a $^{206}Pb/^{238}U$ date >70 Ma and discordance >20% it was removed from the data set, and zircon domains with $^{206}Pb/^{238}U$ dates <70 Ma have ages reported as $^{207}Pb/^{206}Pb$-corrected $^{206}Pb/^{238}U$ dates, with the $^{207}Pb/^{206}Pb$ intercept for correction determined from the Stacey and Kramers (1975) global Pb isotope evolution model. In all samples, the majority of reported zircon U-Pb dates are <60 Ma, with only three samples (SLP200E, SLP200C, SLP200B) yielding a significant fraction of zircon with U-Pb ages >60 Ma (Figure 4). Zircon composition varies widely, specifically showing significant variance in

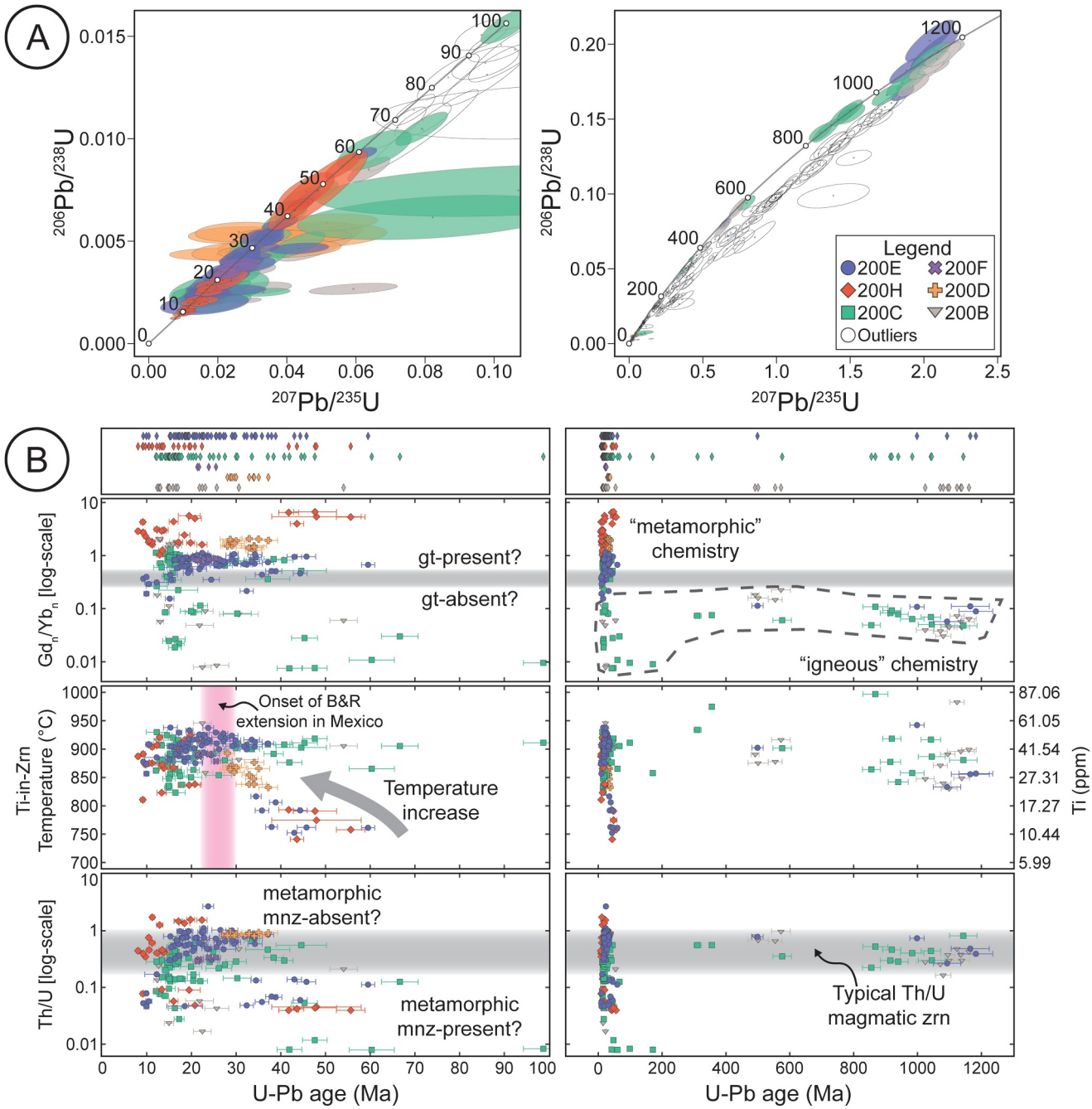

Figure 4. (a) Wetherill concordia plots of zircon with U-Pb ages <100 Ma (left) and all zircon analyses (right), modified from IsoplotR (Vermeesch, 2018). Error ellipses are internal uncertainty (2SE), with analyses colored by sample, and outliers (uncorrected $^{206}Pb/^{238}U$ date >70 Ma and discordance >20%) shown as empty ellipses. (b) Zircon chemical data for interpreted U-Pb ages <100 Ma (left) and all U-Pb age data (right), showing chondrite-normalized Gd/Yb, Ti concentration and Ti-in-Zr temperature estimate (assuming $\alpha TiO_2 = 1$ and $\alpha SiO_2 = 1$; Ferry & Watson, 2007), and Th/U versus U-Pb age, as well the distribution of U-Pb ages for each sample. All data are colored and/or symboled by sample, and all U-Pb age error bars are 2σ.

HREE slopes (Gd_N/Yb_N ranging from 0.006 to 8.66), europium anomalies (Eu/Eu*) ranging from 0.002 to 0.642, Th/U ratios ranging from 0.005 to 2.686, Nb concentrations between 0.017 and 34.8 ppm, and Ti concentrations ranging from 9.50 to 122 ppm. Zircon chemistry for U-Pb ages >60 Ma is relatively constant, but the sub-population with ages <60 Ma shows a significant depletions in HREE (visualized by an increase in Gd_N/Yb_N), much wider variance in Th/U ratios, and a positive younging trend in Ti concentration from ~60 to 25 Ma (Figure 4).

4.3. Mineral Zoning

EPMA EDS/WDS major-element transects and mapping were used to identify major-element zoning in feldspar, rutile, quartz, and garnet. Zircon chemical zoning was assessed through CL imagery. No major-element zonation was observed in feldspar other than plagioclase exsolution lamellae. Rutile exhibits no internal Zr zoning, whereas quartz has significant intragranular Ti zoning over hundreds of microns. Garnet has homogenous major-element (Mg, Fe, Mn, Si, Al) concentrations, except for Ca (Figure 2), which shows core-to-rim increases in grossular mole fractions from 0.34 to 0.38 in the mapped garnet from SLP200E (Droubi et al., 2024). Zircon grains exhibit highly diverse textures, but most commonly display oscillatory-zoned cores sharply bounded by multiple CL-bright to CL-dark mantles/rims that lack internal zoning (Droubi et al., 2024) but correspond to differences in TE composition. Other grains are homogenous in CL brightness with uncommon sharp CL changes along irregular grain boundaries. Finally, some grains appear mostly homogenous in CL, but exhibit faint variability in CL texture that resembles both a "soccer-ball" sector-zoned appearance and relict igneous cores.

The observed TE compositional variation of garnet (Figure 3), even for grains within the same sample, suggests that the complexity of garnet zoning is difficult to interpret with a one-dimensional data set alone. Two garnets, one from SLP200H and one from SLP200E (Figure 2), were chosen for TE grid mapping based on being the largest and most pristine grains in their respective thin sections. After outlier removal in the SLP200E mapped garnet, we observe a HREE-rich interior with concentrations decreasing radially outward (Figure 5, Droubi et al., 2024). Superimposed on this trend is smaller-scale "Island-Moat" zoning, where subhedral zones ("Islands") of garnet are mantled by REE- and HFSE-poor μm-scale bands ("Moats") with no obvious spatial relationship to the broader grains containing them (Figure 5, Droubi et al., 2024). By normalizing each elemental profile or map to elements that undergo similar rates of intracrystalline diffusion in garnet (i.e., using Lu/Gd or Zr/Hf rather than each element individually), the "Island-Moat" zoning is minimized. In contrast to these zoning trends, phosphorus shows a gradual increase in concentration outward of the interior, from <100 ppm to >200 ppm, with areas of elevated concentration (up to 350 ppm) at the garnet rim and a circular, inclusion-rich zone in the interior (Figure 5). The mapped garnet from SLP200H has significant kelyphyte/melt infiltration and fracturing, which were removed from the TE data set. This garnet exhibited the "Island-Moat" zoning texture observed in the garnet from SLP200E, where zones of relatively high concentrations of REE and HFSE show diffusive gradients toward lower concentration, μm-scale domains or "moats" (Droubi et al., 2024). Notably, this garnet has a domain characterized by the presence of sillimanite needle inclusions, and this domain is HFSE-depleted. Phosphorus concentration appears homogenous (~350 ppm) with minor zones of depletion near rims or melt infiltration fractures (Droubi et al., 2024).

5. Discussion

5.1. P-T History

The P-T history of the El Toro metapelite xenoliths is constrained by multiple thermobarometers, as well as phase equilibria modeling, with P-T estimates indicating that these xenoliths resided in the lower crust at UHT conditions prior to eruption (Table 1; Figure 6). In a system of co-existing zircon, rutile, and quartz, the incorporation of Ti into zircon (Crisp et al., 2023; Ferry & Watson, 2007) and quartz (Osborne et al., 2022; Thomas et al., 2010), as well as the incorporation of Zr into rutile (Tomkins et al., 2007), has been experimentally and empirically shown to maintain a reliable temperature record, even at UHT conditions (Ewing et al., 2013; Liu et al., 2010; Meyer et al., 2011; Mitchell & Harley, 2017). Intersecting GASP barometry and 4^+ thermometry (Ti-in-zircon, Zr-in-rutile, Ti-in-quartz) with Monte-Carlo derived uncertainties yields *P-T* estimates of 925–972°C, 0.72–0.85 GPa for all xenoliths that contain mesoperthitic feldspar, and the intersection of the GRAIL barometer and the 4^+ thermometers for sample SLP200D, which contains a single ternary feldspar phase, yields a P-T estimate of 948°C, 0.54 GPa (Table 1; Figure 6).

The pressure estimates of 0.72–0.85 GPa correspond to depths of 26–31 km for samples with mesoperthitic feldspar and pressure estimates of 0.54 GPa correspond to a depth of ~20 km for SLP200D, assuming lithostatic pressures and average crustal density of 2,800 kg/m^3 (Table 1; Figure 6). Independent Zr-in-rutile and Ti-in-quartz thermometry, calculated at 1.0 GPa using the calibrations of Tomkins et al. (2007) and Osborne et al. (2022) gives estimates ranging from 855 to 988°C (Zr-in-rutile) and 880–1,062°C (Ti-in-quartz), respectively (Table 1; Droubi et al., 2024), similar to rutile and quartz trace-element thermometry observed in metapelite xenoliths from Kilbourne Hole (Cipar et al., 2020). Two-feldspar solvus thermometry (Benisek et al., 2010),

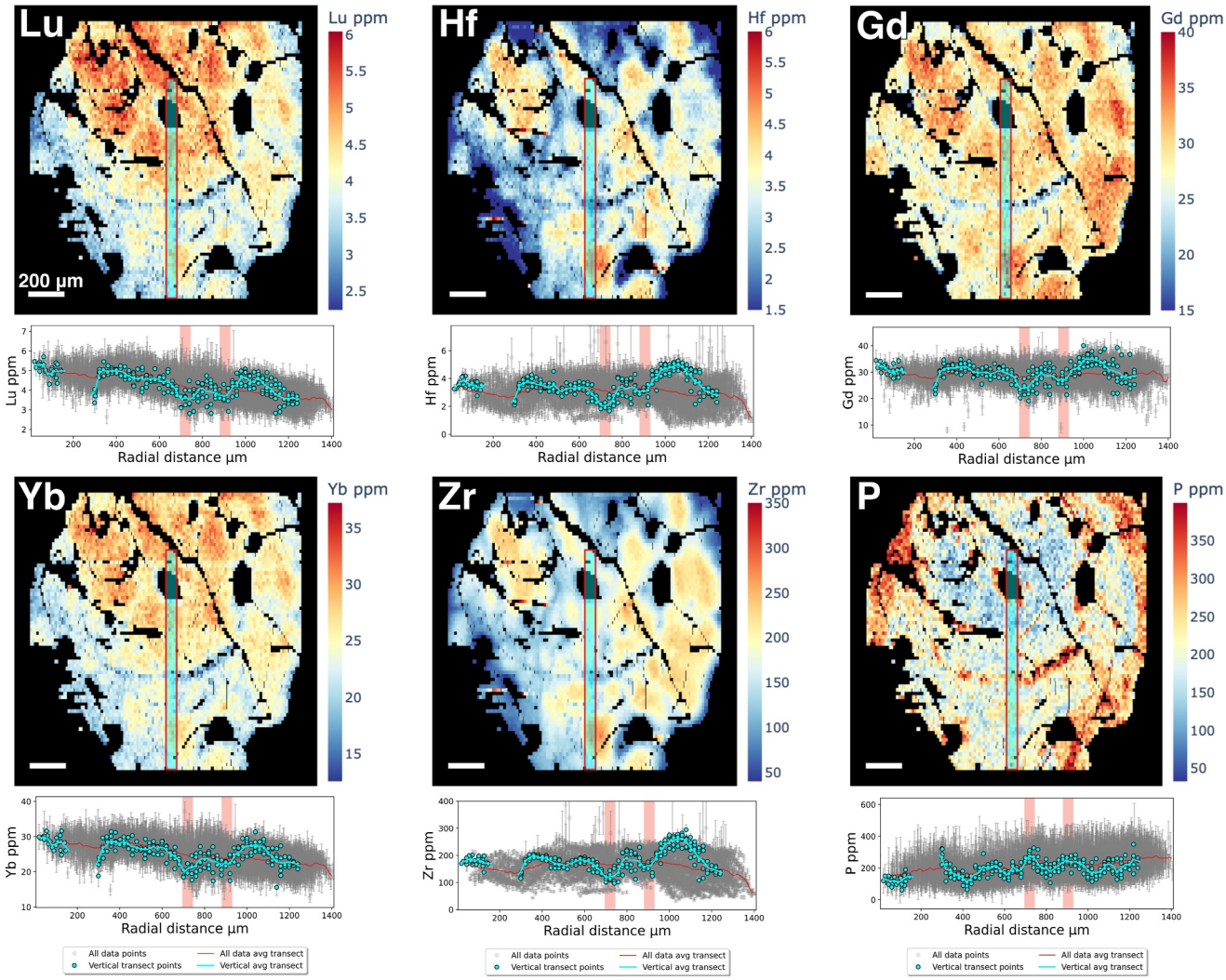

Figure 5. Trace-element maps for the mapped garnet from SLP200E showing intragrain variation in Lu, Yb, Hf, Zr, Gd, and P. Beneath each map is a plot comparing spot concentration to radial distance from hypothesized origin, with all analyses plotted in gray with internal uncertainties, the moving average of all analyses as a function of radial distance in red, and a 1-D transect with analysis points and moving average in blue. Comparison of full data set and 1-D transect plotted in concentration versus radial distance highlights observational differences; the 1-D transect only shows the "Island-Moat" texture, but the full data set smooths out the "Island-Moat" texture, revealing HREE trend.

calculated assuming $P = 1.0$ GPa, suggests that the peak temperatures experienced by samples with mesoperthite, before inferred cooling and development of exsolution lamellae directly prior to eruption, ranged from 900 to 1,060°C, and peak temperature experienced by SLP200D ranged from 840 to 880°C (Table 1; Figure 6). Additionally, maximum Ti-in-zircon temperature estimates for zircon with U-Pb ages <60 Ma within each sample range from 891 to 938°C (Table 1; Figure 6). Gd/Dy-in-garnet barometry (Bea et al., 1997) implies isobaric garnet growth at a pressure range of 0.75–1.09 GPa (Table 1; Figure 6), with similar or higher Gd/Dy-in-garnet pressure estimates (Bea et al., 1997) relative to GASP/GRAIL pressure estimates within each sample (Figure 6) potentially recording minor differences in xenolith depths between peak metamorphism and eruption, or alternatively reflecting systematic calibration offsets. These P-T conditions are supported by Theriak-Domino phase equilibria calculations using the bulk compositional data on the same xenoliths from Pool (1990) (see Supporting Information I in Droubi et al. (2024) for more details), which demonstrate that the inferred peak assemblage and garnet inclusion phase assemblage occur at P-T conditions in excess of 840°C and 0.7 GPa (Figure 6). It should be noted that the GRAIL pressure estimates for SLP200D required additional assumptions about the ilmenite solution model (Droubi et al., 2024) and the results are observably lower than phase equilibria and Gd/Dy-in-garnet pressure estimates, suggesting the GRAIL reaction may not be an accurate barometer for

Table 1
P-T Estimates for El Toro Metapelite Xenoliths

Sample	SLP200E	SLP200C	SLP200F	SLP200H	SLP200D[a]
Intersection P-T (GASP/GRAIL, Zr-in-rutile, Ti-in-quartz)					
Depth (km)[b]	27.7	26.4	26.3	31.1	19.6
P (GPa)	0.76	0.72	0.72	0.85	0.54
2SD (GPa)	0.18	0.16	0.18	0.16	0.16
T (°C)	937	945	925	972	948
2SD (°C)	61	54	59	56	52
Gd/Dy-in-garnet barometry					
P range (GPa)	1.09–0.89	0.89–0.75	0.89–0.75	0.89–0.75	0.75–0.66
Depth range (km)[b]	39.7–32.4	32.4–27.3	32.4–27.3	32.4–27.3	27.3–24.0
Ti-in-zircon thermometry for U-Pb age <60 Ma[c]					
Max T (°C)	938	930	891	925	893
Ternary feldspar solvus thermometry (P = 1.0 Gpa)					
T range (°C)	900–1,060	900–1,060	900–1,060	900–1,060	840–880
Independent Zr-in-rutile thermometry (P = 1.0 Gpa)					
T range (°C)	855–969	865–965	875–957	948–988	930–968
Independent Ti-in-quartz thermometry					
T range (°C)	882–973	900–1,001	880–970	882–998	913–1,062

[a]SLP200D is the only sample where GRAIL barometry was used instead of GASP, using default parameters for ratio of ordered to disordered ilmenite in the "ilmm" solution model. [b]Depth calculated assuming a homogenous crustal density of 2,800 kg m^{-3}. [c]Calibration of Ferry and Watson (2007) assuming $\alpha TiO_2 = 1$ and $\alpha SiO_2 = 1$.

SLP200D. The large pressure uncertainties on the Monte Carlo-derived intersection thermobarometry introduce the possibility that the xenoliths resided in a shallower portion of the crust. However, such shallower depths are at odds with the independent thermobarometry and phase equilibria modeling results, and would require even more extreme crustal geotherms for the continental crust (Figure 6), which are not compatible with surface heat flow estimates (e.g., Cipar et al., 2020). Further details of the thermobarometry and phase equilibria calculations are presented in Droubi et al., 2024.

Based on thermobarometry and phase-equilibria modeling using the observed assemblage of garnet, sillimanite, quartz, mesoperthitic feldspar, rutile, and accessory ilmenite and zircon, the xenoliths are hypothesized to have formed from sediments that, following emplacement into the crust, were isobarically heated to >900°C at >0.72 GPa or >26 km depth (except for SLP200D), just above the geophysically defined Moho (~30–40 km; Peredo et al., 2021) in San Luis Potosi (Figure 6). Phase equilibria modeling and the observation of rounded quartz, feldspar, and sillimanite needles as inclusions in garnet suggest that prograde metamorphism resulted in garnet growth and melt production by the continuous biotite dehydration melting reaction Bt + Als + Pl + Qz = Grt ± Kfs + Lq (all mineral abbreviations follow Warr, 2021) at >800°C (Spear & Kohn, 1996). While thermodynamic calculations suggest that garnet growth prior to melting was possible, no garnet cores contain inclusion-assemblages or remnant major element zonation that would indicate subsolidus garnet growth. This suggests that garnet growth/equilibration under the interpreted melt-present P-T conditions involves erasure of pre-existing garnet histories. Melt production also contributed to the neocrystallization of zircon with garnet-present chemical signatures (Figure 4). While all the products of this reaction are readily observable, the preservation of only minor (<1 vol. %) to no biotite in these samples implies that melt extraction was efficient (White & Powell, 2002). It is important to acknowledge that melt loss would have resulted in a restitic bulk rock composition that is likely not representative of the composition from which the garnet grew, obscuring exact phase equilibria P-T determinations of the biotite dehydration reaction. However, due to the steep Clapeyron curve of the biotite dehydration reaction, changes in the bulk rock composition related to melt loss are expected to only shift the location of the reaction to lower temperatures, and not significantly change the topology of the higher-grade stability fields (White & Powell, 2002). The stability of higher-grade phase reaction topology

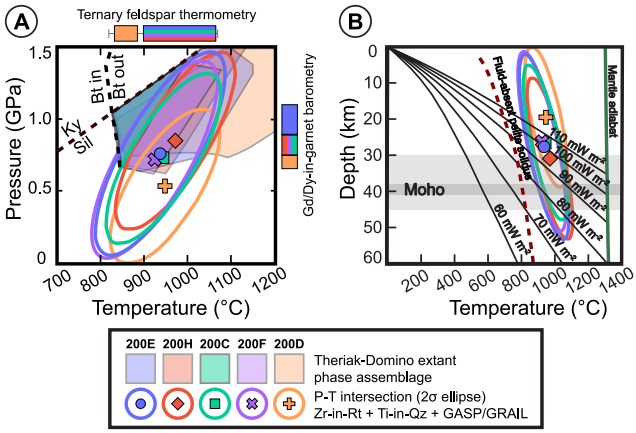

Figure 6. Pressure/depth-temperature points and 2σ error ellipses for the Monte Carlo intersection of Zr-in-Rt, Ti-in-Qz, and GASP/GRAIL thermobarometry overlaid on (a) P-T plot with extant phase assemblage stability fields from phase equilibria modeling, with reactions that are consistent for all five samples, plus ternary feldspar temperature estimates for a pressure range of 0.5–1.0 GPa and Gd/Dy-in-garnet pressure estimates, and (b) depth-temperature plot with estimated Mohorovicic (Moho) discontinuity depth (Peredo et al., 2021), fluid-absent pelite solidus (Vielzeuf & Holloway, 1988), mantle adiabat (McKenzie & Bickle, 1988), and steady-state geotherms (Droubi et al., 2024) for varying surface heat flow, which suggests P-T surface heat flow estimates are in good agreement with geophysical estimates of >70 mW m^{-2} for the Mexican Basin and Range (Cipar et al., 2020 and ref therein).

is demonstrated by consistent overlap in the location of the biotite dehydration reaction for all five modeled samples, despite potential differences in inferred melt extraction (Figure 6). Further, because of the sigmoidal fabric defined by sillimanite needle inclusions (Figure 2), it is inferred that some period of garnet growth was syndeformational (possibly during the onset of regional extension), with deformation likely enhanced by the presence of melt and continuing after garnet growth based on observed subhedral garnet morphologies. Our inference for significant melt loss from the El Toro xenoliths is analogous to that hypothesized for metapelitic Kilbourne Hole xenoliths (Reid, 1990). These interpretations are in agreement with previous studies (Hayob et al., 1989; Solari et al., 2023) suggesting that these xenoliths were derived from a lower crust that experienced a UHT metamorphic event recorded by zircon and garnet growth.

5.2. Zircon Petrochronology

The slow diffusivity of U and Pb (Cherniak & Watson, 2001) and distinct trace-element composition (e.g., Hermann & Rubatto, 2009; Holder et al., 2020; Rubatto, 2002; Taylor et al., 2017; Whitehouse & Platt, 2003; Yakymchuk et al., 2018) of zircon makes it a popular petrochronometer for constraining the timing and temperature of UHT metamorphism (e.g., Cipar et al., 2020; Laurent et al., 2023). Zircon U-Pb dates range from 8.1 Ma to 1,183 Ma, with four chemically and texturally distinct zircon sub-populations interpreted as follows: (a) inherited igneous cores with crystallization ages from ~60 Ma to 1,183 Ma; (b) Cenozoic zircons with "igneous" composition and textures, interpreted as older igneous zircon crystals that underwent partial Pb resetting, thus having decoupled U-Pb and trace-element records; (c) zircons with U-Pb ages spanning ~36–60 Ma with distinct "metamorphic" textures and composition, with minimum Ti-in-zircon temperature estimates of ~740–785°C; and (d) zircons with U-Pb ages ≤30 Ma and "metamorphic" composition and textures consistent with peak UHT metamorphism at ~30 Ma, followed by >15 Myr of peak-T residence or slight but protracted cooling. All Ti-in-zircon temperature estimates are calculated using the calibration of Ferry and Watson (2007) assuming unity for the activities of TiO_2 and SiO_2 (consistent with the extant assemblage), with temperature estimates over the permissible pressure range (0.5–1.0 GPa) within 2.5% of temperature estimates using the calibration of Crisp et al. (2023), which accounts for pressure-dependent Ti-site occupancy in zircon.

The spectrum of inherited concordant zircon analyses–ranging from >60 Ma to 1,183 Ma, with Th/U ratios (Kirkland et al., 2015; Yakymchuk et al., 2018), HREE concentrations (Figure 4), and CL textures (see Droubi et al., 2024) typical of igneous processes–is consistent with their interpretation as detrital igneous grains, also observed by Solari et al. (2023). The relative paucity of zircon zones with compositional characteristics indicative of a metamorphic origin—most notably HREE-depletion (Rubatto, 2002; Rubatto & Hermann, 2007) defined by Gd_n/Yb_n ~0.7 or higher—and dates older than ~60 Ma suggests that these rocks experienced elevated metamorphic temperatures during garnet growth only after ~60 Ma. These data further support the interpretation that granulite-facies metapelite xenoliths from Cerro El Toro are metamorphosed sediments only recently incorporated into the Mexican lower crust, possibly sourced from the subducting Farallon slab, as proposed by Solari et al. (2023). However, we interpret the oldest demonstrably metamorphic zircon age of ~60 Ma (Figure 4) to constrain the earliest time in which these sediments could have been incorporated into the lower crust. A ~60 Ma relamination age is at least 10 Myr older than the mid-Eocene age proposed by Solari et al. (2023) for the same xenoliths, but is more tectonically consistent, as it suggests that the protolith sediments were emplaced into the lower crust during the final stages of compression from the Mexican orogeny (Fitz-Díaz et al., 2018) rather than during a time period when Farallon slab rollback and backarc extension operated in the Mesa Central.

In Wetherill U-Pb concordia space, the outliers define several mixing trends from multiple concordant Precambrian zircon populations that all converge toward intercept dates <60 Ma (Figure 4). This observation, coupled by the emergence of greater compositional and textural variability at <60 Ma (Figure 4), is further consistent with UHT metamorphism only after ~60 Ma. At face value, the presence of two distinct zircon

compositions with U-Pb dates <60 Ma–i.e., those with "metamorphic" composition (flat HREE slopes, depleted Nb, highly variable Th/U, and low Eu/Eu*) and those with "igneous" composition (steep HREE slopes, enriched Nb, typical Th/U, and higher values of Eu/Eu*)–could suggest continuous addition to neocrystallized magmatic zircon during high-grade lower-crustal metamorphism. However, Cenozoic zircon analyses with "igneous" compositions only occur in samples with a significant fraction of inherited ages (SLP200E, SLP200C, SLP200B) (Figure 4), and these young "igneous" zircon spots occur within or adjacent to cores that display CL oscillatory zoning or well-defined, concentric core-rim structures. These zircon textures are commonly interpreted as recording igneous processes, whereas the zircon analyses with "metamorphic" composition typically occur in CL-bright rims or homogenous CL grains. Further, it can be seen that although some of the zircon analyses with $^{207}Pb/^{206}Pb$-corrected U-Pb dates between 40 and 60 Ma with "igneous" composition passed our outlier removal method, they are demonstrably discordant (Figure 4), suggesting additional uncertainty in their U-Pb record. Given the extreme temperature conditions in these rocks over potentially protracted timescales (>20 Myr), intracrystalline volume diffusion of Pb through zircon may have been sufficient to alter the "faithful" U-Pb crystallization age. For example, the characteristic length scale ($x = 2\sqrt{Dt}$) of Pb diffusion through zircon after 20 Myr is 9 μm at 900°C and 87 μm at 1,000°C (Cherniak & Watson, 2001)—and partial resetting could be enhanced by dissolution-reprecipitation recrystallization in the presence of transient melts. Such U-Pb and trace-element or textural decoupling has been observed in other similar UHT rocks (e.g., Štípská et al., 2016). Therefore, we interpret the Cenozoic zircon population with igneous TE characteristics as inherited detrital zircon that have undergone partial Pb resetting, and thus have decoupled U-Pb and TE records. Considering the proposed unreliability of Cenozoic zircon with "igneous" composition, all further interpretations about the recent metamorphic history of these zircons will be based solely on those zircon crystals with demonstrably "metamorphic" compositions, characterized by HREE-depletion (CI-normalized Gd/Yb > 0.7) and U-Pb ages less than <60 Ma, as well as low Eu/Eu* and Nb concentration. This zircon population is interpreted to have been in chemical equilibrium with the observed peak metamorphic assemblage within these xenoliths, and thus the age information that the metamorphic zircon preserves is directly relevant to interpreting the timescales over which peak metamorphism occurred.

Within the metamorphic zircon population, there are two identifiable groups: (a) a sparse group of "older" (~37–60 Ma) zircon grains that are generally larger crystals with low Th/U (≤0.1) and low Ti concentrations (10–15 ppm), and (b) a more abundant group of zircon grains with U-Pb ages <37 Ma distinguished from the older population by having orders of magnitude higher Th/U ratios (>0.1) and Ti concentrations (27–61 ppm). The unique compositions (highest endmember CI-normalized Gd/Yb, extremely low endmember Th/U) and larger grain size of the older population, as well as the absence of inherited cores in the case of SLP200H and SLP200D, preclude this zircon population from representing simple analytical mixing between <37 Ma zircon and inherited cores or partial resetting of an older zircon population (Figure 4). In contrast, the smaller grains with higher Ti contents are interpreted as having equilibrated during younger UHT metamorphism. Our preferred interpretation is that the older metamorphic zircon population preserves a record of granulite-facies metamorphism that predates the onset of Basin and Range extension, likely related to conductive heating in the retro-wedge from asthenospheric upwelling during rollback of the Farallon plate (e.g., Currie & Hyndman, 2006). A sharp increase in Ti-in-zircon temperatures from ~36 to 30 Ma (Figure 4) may signify an increase in asthenospheric input, possibly related to mantle attenuation during slab detachment and removal beneath the Mesa Central. The 10–15 ppm Ti concentrations correspond to Ti-in-zircon temperature estimates as low as ~740–785°C, which demonstrates that the lower crust was not yet at UHT over this interval. Further, the extremely low Th/U ratios over this interval are interpreted as metamorphic zircon growth in the presence of monazite (Yakymchuk et al., 2018), consistent with global observations of monazite stability in similar metasediments at similar temperatures (e.g., Alessio et al., 2018; Williams et al., 2022; Wyatt et al., 2022). Between 35 and 25 Ma, zircon Ti concentrations and Th/U ratios increased significantly, which is interpreted as the approximate time of crustal heating to UHT (as high as ~946°C, using the highest observed Ti-in-zircon of 59.3 ppm) (Figure 4). The extreme increase in zircon Th/U at peak metamorphism is interpreted as temperatures crossing the monazite solubility threshold (Williams et al., 2022), leading to a Th/U maximum in zircon before further melting and zircon crystallization at UHT exhausted the available Th and decreased Th/U in subsequently crystallizing zircon (Figure 4) (Yakymchuk et al., 2018). The zircon petrochronologic data are consistent with >15 Myr of lower crustal, garnet-present zircon crystallization at UHT, either isothermally or by slow cooling (<10°C/Myr), coincident with the onset of Basin and Range extension in Mesa Central (Henry & Aranda-Gomez, 1992). This interpretation is analogous to

xenolith-based interpretations for lower-crustal thermal histories from Kilbourne Hole, USA (Cipar et al., 2020; Scherer, 1999; Scherer et al., 1997), which report zircon and garnet geochronology dates coincident with Basin and Range extension.

Given the abundant textural and compositional divisions between metamorphic and igneous origins for the zircon in this study, the similarity in Ti content between these zircon populations is unexpected. Most igneous zircons crystallize at lower temperatures (550–750°C) than those expected at granulite-facies conditions (750–1,000°C), resulting in detrital zircon with more modest Ti contents than those reported here (e.g., Fu et al., 2008). One explanation for elevated detrital zircon Ti contents is that the initial zircon Ti contents have partially re-equilibrated during Cenozoic UHT metamorphism. Recent experimental work on Ti diffusion in zircon (Bloch et al., 2022) has demonstrated that Ti diffusion parallel to the zircon c-axis is orders of magnitudes faster than previous estimates perpendicular to the c-axis (Cherniak & Watson, 2007). Using new Arrhenius parameters for c-axis parallel Ti diffusion (Bloch et al., 2022), characteristic length scales of diffusion ($x = 2\sqrt{Dt}$) for Ti are 102 μm for 20 Myr at 900°C and 952 μm for 20 Myr at 1,000°C, which would readily facilitate re-equilibration of low-Ti detrital zircon to higher Ti contents for expected timescales of crustal heating in these rocks. This hypothesis is further supported by the observation that the lowest Ti contents in the entire data set were measured in the ∼37–60 Ma zircon with large (>200 μm) metamorphic zircon cores (e.g., zircon SLP200H_lg_4, Droubi et al., 2024).

In sum, the zircon data, augmented by P-T determinations, support the following tectonothermal history for the Mexican Basin and Range lower crust: (a) sediments were incorporated into the lower crust by 60 Ma; (b) between 37 and 60 Ma, the lower crust reached temperatures ≥740°C, associated with asthenospheric upwelling during transition to a backarc extensional setting; (c) the lower crust underwent a sharp increase in temperature from granulite-facies to UHT, possibly related to slab detachment and removal beneath the Mesa Central and a transition from localized backarc extension to Basin and Range extension; (d) finally, by ∼30 Ma, the lower crust reached peak temperatures of >900°C, where it remained– either isothermally or by slow cooling (<10°C/Ma)– for over 15 Myr throughout regional extension. Unlike lower-crustal xenoliths from Kilbourne Hole (Cipar et al., 2020), the El Toro zircon data do not extend to dates younger than ∼8 Ma, however the extant metamorphic assemblages and quantitative P-T data from these xenoliths support the persistence of UHT conditions to the modern.

5.3. Garnet Diffusion Chronometry

Garnet trace-element transects and mapping (George et al., 2018; Rubatto et al., 2020) are commonly used to interpret metamorphic histories (see Baxter et al., 2017), with several well-documented mechanisms to explain distinct garnet trace-element distributions (Ague & Axler, 2016; Bloch et al., 2020; George et al., 2018; Hirsch et al., 2003; Konrad-Schmolke et al., 2008, 2022; Otamendi et al., 2002; Skora et al., 2006). If garnet has indeed been present in the metasedimentary lower crust of north-central Mexico since the onset of UHT conditions, then the observed garnet compositional zoning should provide critical information on the duration and heat transfer mechanisms responsible for UHT metamorphism. Intracrystalline major-element distributions in garnet are homogenous except for minor core-to-rim (500 μm) grossular zoning of 0.34–0.38 mol fraction in the mapped garnet from SLP200E (Figure 2; Droubi et al., 2024). Based on the elevated dP/dT of grossular isopleths calculated for this sample (Droubi et al., 2024), this zonation is interpreted as a high-temperature cooling trend that occurred prior to eruption of Cerro El Toro, contemporaneous with development of exsolution lamellae in feldspar. Indeed, the preservation of Ca zoning in garnet over a length scale of ∼1,000 μm in a rock that experienced a peak metamorphic temperature >900°C implies that the cooling interval responsible for zoning likely occurred for no longer than ∼5 Myr prior to eruption (Caddick et al., 2010, their Figure 2b). The observed trace-element zoning in the garnet grains from these xenoliths, specifically the mapped garnet from SLP200E, support the hypothesis that garnet has been compositionally modified by two processes since growth. First, the observed radial HREE-depletion in the mapped garnet from SLP200E (Figure 5) is interpreted as a primary growth signature that has undergone partial diffusive relaxation. Another observation in many garnet crystals from the Cerro El Toro xenoliths are the "Island-Moat" textures of subhedral zones of garnet that show diffusive loss of REE and HFSE along μm-scale bands. These "Island-Moat" textures are visually co-located with abundant kelyphyte fractures and veins in the garnet, leading to the interpretation that the "moats" are areas that have experienced melt/fluid infiltration and garnet annealing. This melt/fluid infiltration is hypothesized to have

occurred just prior to eruption due to the preservation of these μm-scale compositional gradients in REE + HFSE despite UHT conditions. Likewise, the circular annulus of increased phosphorus concentration in the interior of the mapped garnet from SLP200E is interpreted as recent melt/fluid infiltration related to pre-eruptive processes, possibly utilizing pre-existing weaknesses from growth features. This interpretation is based on the similarity of the annulus to phosphorus rim zoning with visible fracture/infiltration features (Figure 5). Finally, because the "Island-Moat" textures are also observed in garnet from Kilbourne Hole xenoliths (Figure 7), this process is inferred to have affected lower crustal garnet widely throughout the Basin and Range (Figure 1), with pre-eruptive modification being the simplest hypothesis.

If we assume that the "Island-Moat" trace-element zoning textures in garnet from El Toro and Kilbourne Hole xenoliths occurred at UHT conditions and originally formed sharp, step-function boundaries between "islands" and "moats," we can use these features to constrain permissible timescales of pre-eruptive fluid and/or melt infiltration in the lower crust. To do so, 20-μm wide concentration profiles of Lu and Hf were extracted from "Island-Moat" transects within mapped garnet from SLP200E and DEKH2 using the CellSpace Image function in Iolite v4.7 (Paton et al., 2011) and modeled using the Diffuser web application (Wu et al., 2022). Using the Lu and Hf diffusion parameters of Bloch et al. (2020) as reported in the Diffuser database (updated 16 May 2023; Wu et al., 2022; Wu et al., pers. comm.), and modeling isothermal diffusion at 50°C intervals from 800 to 1,050°C, the maximum duration for diffusion was calculated from the diffusion profile fits for each transect, with $R^2 > 0.92$ for all diffusion profile fits (Figure 7). Results from this modeling indicate that regardless of published diffusivity parameter choice, at temperatures >850°C, the maximum time estimates for diffusion to occur are less than or equal to 1 Myr (Figure 7). The possibility that the thin sections were cut to expose non-central sections through the garnet, making an elongated chemical profile, as well as the possibility that the initial boundary was not a step-function both further emphasize that these durations should be treated as maximum estimates. These estimates support the hypothesis that "Island-Moat" zoning in lower crustal garnets is a product of rapid (<1 Myr) pre-eruptive processes, similar to pre-eruptive modification observed in phases within other lower-crustal xenoliths globally (e.g., Apen et al., 2022).

To test the hypothesis that the preserved radial core-to-rim HREE zoning in the mapped garnet crystal from SLP200E (Figure 5) is a product of prograde growth and diffusion, with the aim of placing temporal estimates on its formation, a numerical finite volume method modified from Hesse (2012) was used to model the combined effects of crystal growth and volume diffusion on radial concentrations of Lu through garnet. Our modifications to the code provided in Hesse (2012) were to account for thermally mediated volume diffusion following termination of mineral growth from a melt as dictated by Rayleigh fractionation (Hollister, 1966). In the model, diffusion of Lu through garnet was assumed to occur during and after isothermal growth by either the "fast" or "slow" intracrystalline REE diffusion mechanism of Bloch et al. (2020), with an assumed starting melt Lu composition of 0.84 ppm (SLP200E bulk rock INAA value; Pool, 1990) and garnet/melt Lu partition coefficients ranging from 10 to 100. Melt Lu diffusivity was modeled using the Arrhenius parameters from Holycross and Watson (2016, 2018). Further details of the modeling calculations are provided in Droubi et al., 2024. Model calculations indicate that higher temperatures or longer model durations lead to increasing extents of diffusive relaxation (as expected). When using the "fast" Lu diffusion mechanism (Bloch et al., 2020), diffusion chronometry estimates show best fits with the observed radial HREE-depletion at $\log_{10}(D_{Lu}t)$ of 17.7–18 (cm^2) (Figure 8). Though solutions are non-unique, these length-scales of diffusion are consistent with isothermal heating at ∼800°C for ∼10 Myr, 900°C for ∼1 Myr, or a short (0.1 to <1 Myr) pulse of 1,000°C (Figure 8). In contrast, the "slow" Lu diffusion mechanism of Bloch et al. (2020) constrains the time-integrated diffusivity ($\log_{10}(D_{Lu}t)$) to 15.9–16.2 (cm^2) (Figure 8), equating to isothermal residence at ∼800°C for >30 Myr, 900°C for ∼30 Myr, or 1,000°C for ∼5 Myr (Figure 8). Choice of the "fast" or "slow" Lu diffusion mechanisms (Bloch et al., 2020), which represent the end-member Lu diffusivities at the modeled temperature range of 800–1,000°C (Droubi et al., 2024), creates a dichotomy of solutions where invocation of the "fast" Lu diffusion mechanism suggests that observed Lu zoning would not be preserved after ∼10 Myr at the inferred P-T conditions, even by the most conservative temperature estimates, but invocation of the "slow" Lu diffusion mechanism suggests that the observed Lu zoning could have been established within 5–30 Myr at the inferred P-T conditions.

The preservation of garnet trace-element zoning (Figure 5) in rocks that experienced a thermal history of protracted UHT provides a novel opportunity to empirically assess the applicability of the "fast" and "slow" mechanisms of REE diffusion through garnet (e.g., Bloch et al., 2020). The radial HREE zoning in garnet is interpreted and modeled as diffusively relaxed primary growth zoning that has thermally diffused by the "fast" or

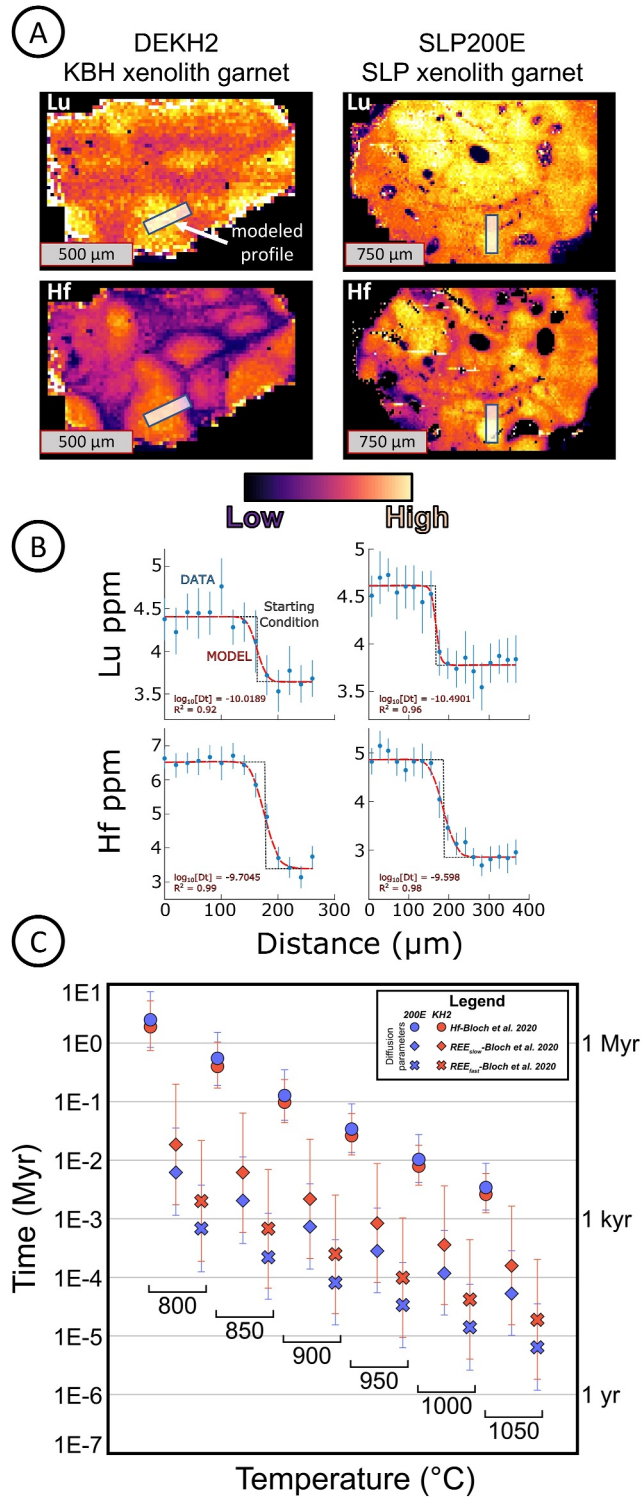

Figure 7. Diffusion modeling of Lu and Hf "Island-Moat" textures in garnet from Kilbourne Hole (KBH), NM, USA sample DEKH2 (Cipar et al., 2020) and El Toro metapelite sample SLP200E, using Diffuser web app (update 16 May 2023; Wu et al., 2022). (a) Lu and Hf maps and profiles for garnets with (b) profile fits, and (c) time versus temperature plot showing maximum time-scale estimates, 2σ uncertainty, form SLP200E (blue) and DEKH2 (red) with choice of web app supplied diffusion parameter represented by differing symbology (circle-Hf, diamond-REE$_{slow}$, X-REE$_{fast}$; Bloch et al., 2020).

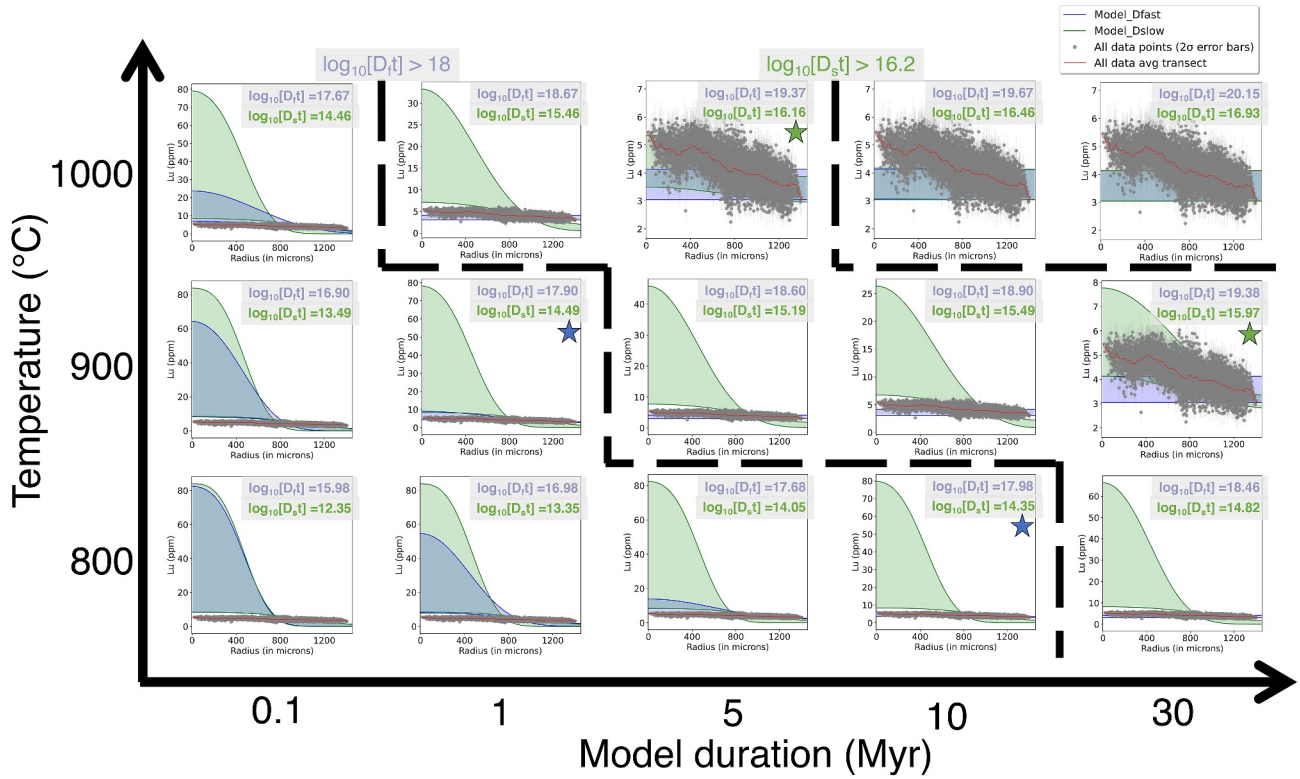

Figure 8. Finite volume model results for changes in SLP200E mapped garnet Lu concentration as a result of isothermal growth and diffusion, using the "fast" (blue) or "slow" (green) rare-earth element diffusion mechanism of Bloch et al. (2020). Resulting plots show the envelope of possible core-to-rim Lu concentration profiles using the various modeling parameters, following a growth period of 0.1 Myr, nested in the larger coordinate space by respective T-t parameter dictating isothermal history of growth and diffusion. Results indicate that higher temperature or longer model duration led to increasing degrees of diffusive relaxation and length-scale of diffusion <Dt>. Best fits for model results compared to the Lu transect from the mapped garnet suggest $\log_{10}$(Dt) was 17.7–18 (cm^2) for the "fast" mechanism and 15.9–16.2 (cm^2) for the "slow" mechanism, with stars indicating plausible isothermal histories.

"slow" Lu diffusion mechanisms of Bloch et al. (2020). These modeling results imply time-integrated magnitudes of diffusion ($\log_{10}(D_{Lu}t)$) of 17.7–18 (cm^2) or 15.9–16.2 (cm^2), respectively (Figure 8), which can be conceptually compared to non-unique temperature-time paths over 25 Myr, or since garnet has been present as indicated by the zircon record (Figure 9). Within this framework, only garnet growth-diffusion calculations that assume "slow" Lu diffusion as the dominant mechanism produce thermal histories that are compatible with the zircon record (Figure 9).

The agreement between the zircon petrochronologic record and garnet diffusion chronometry using the "slow" Lu diffusion mechanism (Bloch et al., 2020) aligns with the recommendation by Bloch et al. (2020), that the "slow" mechanism dictates elemental Lu diffusion in natural garnet crystals. Accordingly, garnet data from this study provides an empirical confirmation that even at UHT conditions and lower-crustal pressures, the "slow" Lu diffusion mechanism is the dominant mechanism in garnet. Further, results from garnet diffusion chronometry lend confidence toward the fidelity of the zircon petrochronologic record within the xenoliths, despite concerns about anisotropic Ti diffusion in zircon. If the Ti record were impacted by the significant anisotropy in diffusion of Ti in zircon (Bloch et al., 2022) this could result in much faster re-equilibration of peak-UHT zircon Ti concentrations to lower concentration, younger zircon rims. This would have the result of lowering maximum Ti concentrations of metamorphic zircon–presumably with U-Pb ages ~35–25 Ma–and raising the Ti concentrations of younger zircon that may have crystallized at lower temperatures. However, agreement with the garnet diffusion chronometry, the large number of zircon analyses with detailed textural characterization, and the well-established nature of the zircon method used by this study (e.g., Cipar et al., 2020) all support that the record of Ti in metamorphic zircon is accurately preserved in our samples.

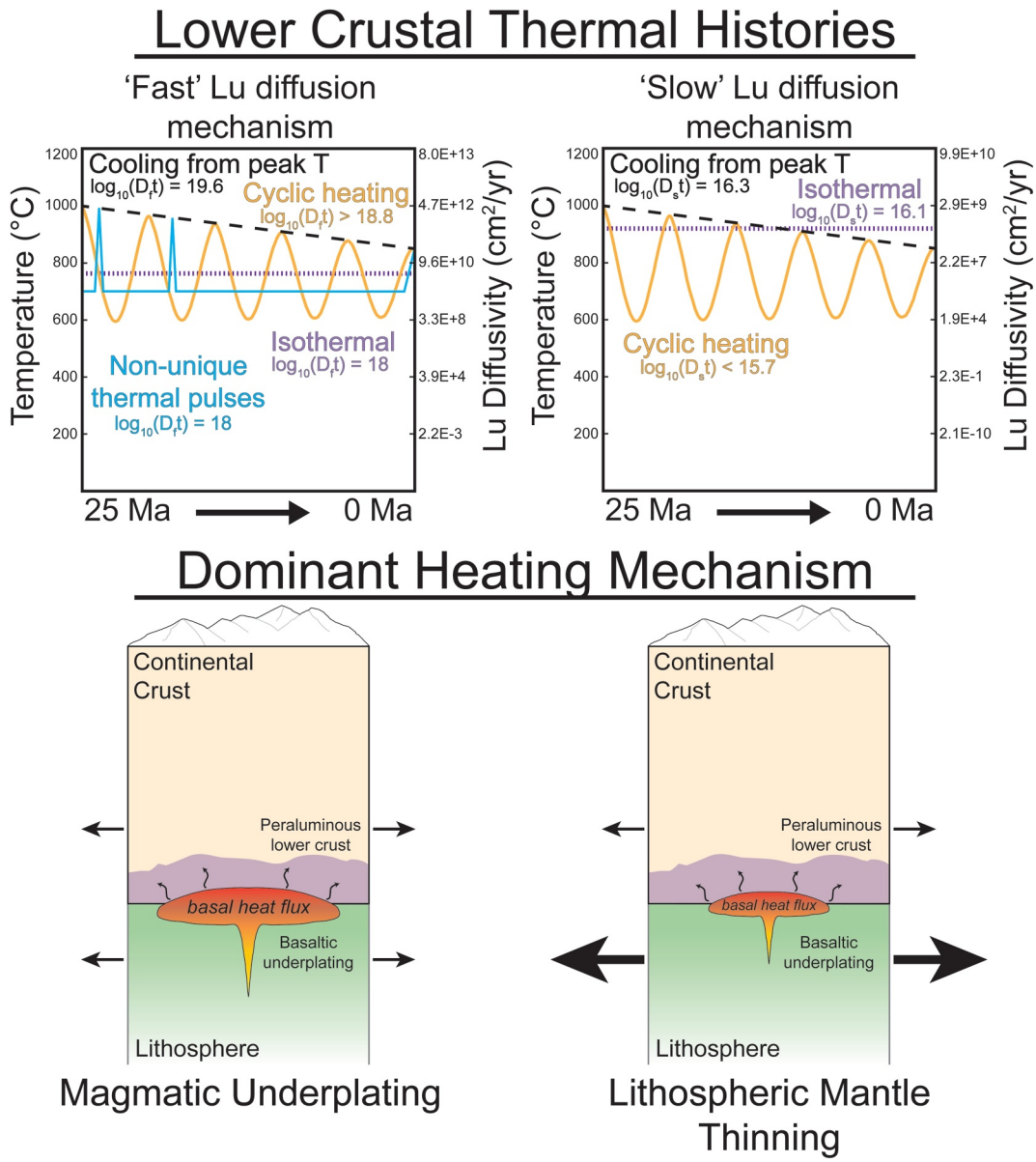

Figure 9. (Top) Visualization of possible T-$D_{Lu\text{-}in\text{-}garnet}$-t paths for the Quaternary lower crustal thermal history of Cerro El Toro, using the "fast" or "slow" rare-earth element diffusion mechanisms of Bloch et al. (2020) to compare a linear cooling history, a punctuated linear cooling ("cyclic") history, an isothermal history, and/or a thermal history defined by rapid (<1 Myr) pulses. The length-scale of Lu-in-garnet diffusion is calculated for the cooling histories, but the isothermal and pulsed histories were constructed to agree with diffusion length-scales from garnet Lu finite volume modeling (Figure 8). (Bottom) Conceptual diagram, motivated by model results and observations, for the preferred interpretation of dominant heat transport mechanisms. The recommended choice of the "slow" Lu diffusion mechanism implies that an elevated heat flux from the mantle into the lowermost continental crust is the dominant method of heat transport.

5.4. Implications for Heat Transfer Mechanisms Driving UHT

Any proposed geodynamic mechanism for the attainment of UHT conditions in the Mesa Central lower crust must be able to reconcile the different mineral records preserved in these rocks. Specifically, the proposed mechanism must account for the following interpretations: (a) peak metamorphic conditions were >900°C at >0.7 GPa, with a peak assemblage consisting of quartz, sillimanite, feldspar, garnet, rutile, and accessory ilmenite and zircon, (b) metamorphic zircon crystallized continuously from at least ~25 Ma until eruption, (c) metamorphic zircon Ti concentrations suggest that UHT conditions peaked around ~30 Ma and persisted through or cooled only slightly

before eruption, (d) zircon TE suggest that garnet has been present from at least ∼25 Ma until eruption, and (e) preserved garnet TE zoning suggests constant temperature or slow linear cooling since the onset of UHT between ∼25 and 35 Ma, as well as rapid (<1 Myr) TE-modifying processes directly prior to eruption of Cerro El Toro.

The degree of similarity between the thermal history afforded by these constraints and that derived for the lower crust beneath the southern portion of the Rio Grande Rift (Cipar et al., 2020)–despite greater than 1,000 km of physical separation—is remarkable. While it is likely that thinning of the mantle lithosphere and magmatic underplating are both active processes in the Basin and Range lower crust, the persistence of UHT for >15 Myr, as recorded by the Ti-in-zircon record and supported by garnet diffusion chronometry in the El Toro xenoliths, implies a protracted, elevated heat flux across the Moho, with timescales more consistent with conductive heat flow as the dominant heating mechanism, compared to local emplacement of mantle-derived magmas. Conduction as the dominant heat flow mechanism is tectonically consistent with sustained removal and/or attenuation of the lithospheric mantle beneath the Mesa Central during regional extension (Figure 4b).

Further, the small subset of metamorphic zircon data from ∼60 Ma to 37 Ma with Ti-in-zircon temperature estimates of ∼740–785°C suggests that the Mesa Central lower crust underwent heating to granulite-facies metamorphic conditions concomitant with the transition from backarc compression to backarc extension and prior to heating to peak UHT conditions–from ∼36–30 Ma. We speculate that this earlier granulite facies metamorphism drove partial melting and melt removal, thermally priming peraluminous lower crust for the attainment of UHT conditions (e.g., Schorn et al., 2018).

6. Conclusions

This study presents new data on lower crustal metapelite xenoliths from the Quaternary cinder cone Cerro El Toro (San Luis Potosí, Mexico) that augments existing interpretations of the recent metamorphic history of the lower crust in Mexico and the geodynamic mechanisms responsible for UHT in the Basin and Range. Data from this study indicates that the peraluminous component of the Mexican lower crust formed from sediments that were incorporated into the lower crust by approximately 60 Ma, though the specific mechanism by which this occurred is as yet unknown. Pressure-temperature constraints and zircon petrochronology suggest that during the transition from backarc compression to extension in the Mesa Central, between 60 and 37 Ma, the lower crust reached temperatures ≥740°C. Coincident with possible slab foundering and the onset of Basin and Range extension, between ∼36 and 30 Ma, the lower (>26 km depth) crust was isobarically heated to >900°C, with the zircon and garnet record suggesting it remained at these temperatures for >15 Myr until eruption of Cerro El Toro. Phase equilibria modeling results for the preserved assemblage of these xenoliths suggests heating of the lower crust to >900°C resulted in the production of garnet and melt predominantly through a biotite dehydration reaction. The peak assemblage preservation within these rocks indicates that any melt produced during peak metamorphism has since been lost; combined with the zircon geochronology, this implies over 15 Myr of anatexis in the Mexican lower crust, similar to conclusions drawn from Kilbourne Hole, New Mexico (Cipar et al., 2020). Trace-element zoning in garnet suggests a complex history, with partially preserved growth-related HREE profiles leading to diffusion chronometry estimates in agreement with zircon petrochronologic estimates, that is, that garnet crystallized prior to ∼25 Ma. These partially preserved Rayleigh-fractionation profiles are further overprinted by "Island-Moat" trace-element zoning, suggesting rapid (<1 Myr) fluid-mobilization of TE along rapidly annealed fractures in garnet directly prior to eruption of Cerro El Toro, signifying that despite extreme ambient temperatures garnet preserves compositional records of tectonism and volcanism. The relatively young UHT metamorphism recorded by the El Toro xenoliths serves as a modern analog for much older granulite terranes. By constraining the timing and duration of synextensional UHT and anatexis in these xenoliths, as well as the fidelity of the mineral records within, we provide new insight into understanding the preservation of peak-metamorphic assemblages, the modulation of crustal rheology, and the drivers of crustal differentiation in the lower crust beneath southwestern North America in the modern era, as well as granulite terranes around the world.

Data Availability Statement

Samples can be accessed from the James F. Luhr collection at the Smithsonian. All data, software, and model parameters supporting the conclusions in this paper are freely available online (Droubi et al., 2024).

Acknowledgments
This work is supported by National Science Foundation Award EAR-2025122 to A.J.S. SLP xenoliths were collected by G.B. Pool in 1989 and were loaned to J.H. C. and A.J.S. by the Smithsonian from the James F. Luhr collection. We would like to thank editor M. Dekkers, the associate editor, and three reviewers: E. Bloch, M. Williams, and an anonymous reviewer for reviews that significantly improved and clarified this manuscript. The LionChron facility is supported by funds from Penn State. Thanks to M. Feineman and J. Thomas for EPMA assistance.

References

Ague, J. J., & Axler, J. A. (2016). Interface coupled dissolution-reprecipitation in garnet from subducted granulites and ultrahigh-pressure rocks revealed by phosphorous, sodium, and titanium zonation. *American Mineralogist*, *101*(7), 1696–1699. https://doi.org/10.2138/am-2016-5707

Aguirre-Díaz, G. J., Labarthe-Hernández, G., Tristán-González, M., Nieto-Obregón, J., & Gutiérrez-Palomares, I. (2008). The ignimbrite flare-up and graben calderas of the Sierra Madre Occidental, Mexico. *Developments in Volcanology*, *10*, 143–180.

Alessio, K. L., Hand, M., Kelsey, D. E., Williams, M. A., Morrissey, L. J., & Barovich, K. (2018). Conservation of deep crustal heat production. *Geology*, *46*(4), 335–338. https://doi.org/10.1130/g39970.1

Annen, C., & Sparks, R. S. J. (2002). Effects of repetitive emplacement of basaltic intrusions on thermal evolution and melt generation in the crust. *Earth and Planetary Science Letters*, *203*(3–4), 937–955. https://doi.org/10.1016/s0012-821x(02)00929-9

Apen, F. E., Rudnick, R. L., Ionov, D. A., Cottle, J. M., Moyen, J. F., Golovin, A. V., & Korsakov, A. V. (2022). Heat transfer and production in cratonic continental crust: U-Pb thermochronology of xenoliths from the Siberian Craton. *Geochemistry, Geophysics, Geosystems*, *23*(10), e2022GC010497. https://doi.org/10.1029/2022gc010497

Aranda-Gómez, J., & Luhr, J. F. (1996). Origin of the Joya Honda maar, San Luis Potosi, Mexico. *Journal of Volcanology and Geothermal Research*, *74*(1–2), 1–18. https://doi.org/10.1016/s0377-0273(96)00044-3

Aranda-Gomez, J. J., Housh, T. B., Luhr, J. F., Noyola-Medrano, C., & Rojas-Beltrán, M. A. (2010). Origin and formation of neck in a basin landform: Examples from the Camargo volcanic field, Chihuahua (Mexico). *Journal of Volcanology and Geothermal Research*, *197*(1–4), 123–132. https://doi.org/10.1016/j.jvolgeores.2009.08.004

Aranda-Gomez, J. J., Luhr, J. F., Housh, T. B., Conner, C. B., Becker, T., & Henry, C. D. (2003). Synextensional Pliocene-Pleistocene eruptive activity in the Camargo volcanic field, Chihuahua, Mexico. *Geological Society of America Bulletin*, *115*, 298–313. https://doi.org/10.1130/0016-7606(2003)115<0298:sppeai>2.0.co;2

Aranda-Gómez, J. J., Luhr, J. F., Housh, T. B., Valdez-Moreno, G., & Chávez-Cabello, G. (2007). *Late Cenozoic intraplate-type volcanism in central and northern México: A review* (Vol. 422, p. 93). Geology of México: Celebrating the Centenary of the Geological Society of México.

Aranda-Gómez, J. J., Luhr, J. F., & Pier, G. (1992). The La Breña—El Jagüey Maar Complex, Durango, México: I. Geological evolution. *Bulletin of Volcanology*, *54*(5), 393–404. https://doi.org/10.1007/bf00312321

Arzi, A. A. (1978). Critical phenomena in the rheology of partially melted rocks. *Tectonophysics*, *44*(1–4), 173–184. https://doi.org/10.1016/0040-1951(78)90069-0

Audétat, A., Miyajima, N., Wiesner, D., & Audinot, J. N. (2021). Confirmation of slow Ti diffusion in quartz by diffusion couple experiments and evidence from natural samples. *Geology*, *49*(8), 963–967. https://doi.org/10.1130/g48785.1

Audétat, A., Schmitt, A. K., Njul, R., Saalfeld, M., Borisova, A., & Lu, Y. (2023). New constraints on Ti diffusion in quartz and the priming of silicic volcanic eruptions. *Nature Communications*, *14*(1), 4277. https://doi.org/10.1038/s41467-023-39912-5

Barboza-Gudiño, J. R., Zavala-Monsiváis, A., Venegas-Rodríguez, G., & Barajas-Nigoche, L. D. (2010). Late Triassic stratigraphy and facies from northeastern Mexico: Tectonic setting and provenance. *Geosphere*, *6*(5), 621–640. https://doi.org/10.1130/ges00545.1

Baxter, E. F., Caddick, M. J., & Dragovic, B. (2017). Garnet: A rock-forming mineral petrochronometer. *Reviews in Mineralogy and Geochemistry*, *83*(1), 469–533. https://doi.org/10.2138/rmg.2017.83.15

Bea, F., Montero, P., Garuti, G., & Zacharini, F. (1997). Pressure-dependence of rare Earth element distribution in amphibolite- and granulite-grade garnets. A LA-ICP-MS study. *Geostandards Newsletter*, *21*(2), 253–270. https://doi.org/10.1111/j.1751-908X.1997.tb00674.x

Benisek, A., Dachs, E., & Kroll, H. (2010). A ternary feldspar-mixing model based on calorimetric data: Development and application. *Contributions to Mineralogy and Petrology*, *160*(3), 327–337. https://doi.org/10.1007/s00410-009-0480-8

Bird, P. (1979). Continental delamination and the Colorado Plateau. *Journal of Geophysical Research*, *84*(B13), 7561–7571. https://doi.org/10.1029/jb084ib13p07561

Blackwell, D., Richards, M., Frone, Z., Ruzo, A., Dingwall, R., & Williams, M. (2011). Temperature-at-depth maps for the conterminous US and geothermal resource estimates. *GRC Transactions*, *35*(GRC1029452).

Blackwell, D. D., & Richards, M. (2004). Calibration of the AAPG geothermal survey of North America BHT data base. *AAPG Annual Meeting*, 87616. Dallas, Tx, paper.

Bloch, E., Ganguly, J., Hervig, R., & Cheng, W. (2015). 176 Lu–176 Hf geochronology of garnet I: Experimental determination of the diffusion kinetics of Lu 3+ and Hf 4+ in garnet, closure temperatures and geochronological implications. *Contributions to Mineralogy and Petrology*, *169*(2), 1–18. https://doi.org/10.1007/s00410-015-1109-8

Bloch, E. M., Jollands, M. C., Devoir, A., Bouvier, A. S., Ibañez-Mejia, M., & Baumgartner, L. P. (2020). Multispecies diffusion of yttrium, rare earth elements and hafnium in garnet. *Journal of Petrology*, *61*(7), egaa055. https://doi.org/10.1093/petrology/egaa055

Bloch, E. M., Jollands, M. C., Tollan, P., Plane, F., Bouvier, A. S., Hervig, R., et al. (2022). Diffusion anisotropy of Ti in zircon and implications for Ti-in-zircon thermometry. *Earth and Planetary Science Letters*, *578*, 117317. https://doi.org/10.1016/j.epsl.2021.117317

Bown, J. W., & White, R. S. (1995). Effect of finite extension rate on melt generation at rifted continental margins. *Journal of Geophysical Research*, *100*(B9), 18011–18029. https://doi.org/10.1029/94jb01478

Brown, M. (2013). Granite: From genesis to emplacement. *Geological Society of America Bulletin*, *125*(7–8), 1079–1113. https://doi.org/10.1130/b30877.1

Bürgmann, R., & Dresen, G. (2008). Rheology of the lower crust and upper mantle: Evidence from rock mechanics, geodesy, and field observations. *Annual Review of Earth and Planetary Sciences*, *36*(1), 531–567. https://doi.org/10.1146/annurev.earth.36.031207.124326

Caddick, M. J., Konopásek, J., & Thompson, A. B. (2010). Preservation of garnet growth zoning and the duration of prograde metamorphism. *Journal of Petrology*, *51*(11), 2327–2347. https://doi.org/10.1093/petrology/egq059

Cameron, K. L., & Ward, R. L. (1998). Xenoliths of Grenvillian granulite basement constrain models for the origin of voluminous Tertiary rhyolites, Davis Mountains, west Texas. *Geology*, *26*(12), 1087–1090. https://doi.org/10.1130/0091-7613(1998)026<1087:xoggbc>2.3.co;2

Centeno-García, E. (2017). Mesozoic tectono-magmatic evolution of Mexico: An overview. *Ore Geology Reviews*, *81*, 1035–1052. https://doi.org/10.1016/j.oregeorev.2016.10.010

Cherniak, D., & Watson, E. B. (2007). Ti diffusion in zircon. *Chemical Geology*, *242*(3–4), 470–483. https://doi.org/10.1016/j.chemgeo.2007.05.005

Cherniak, D. J. (2010). Diffusion in accessory minerals: Zircon, titanite, apatite, monazite and xenotime. *Reviews in Mineralogy and Geochemistry*, *72*(1), 827–869. https://doi.org/10.2138/rmg.2010.72.18

Cherniak, D. J., Manchester, J., & Watson, E. B. (2007). Zr and Hf diffusion in rutile. *Earth and Planetary Science Letters*, *261*(1–2), 267–279. https://doi.org/10.1016/j.epsl.2007.06.027

Cherniak, D. J., & Watson, E. B. (2001). Pb diffusion in zircon. *Chemical Geology*, *172*(1–2), 5–24. https://doi.org/10.1016/s0009-2541(00)00233-3

Cherniak, D. J., Watson, E. B., & Wark, D. A. (2007). Ti diffusion in quartz. *Chemical Geology*, *236*(1–2), 65–74. https://doi.org/10.1016/j.chemgeo.2006.09.001

Cipar, J. H., Garber, J. M., Kylander-Clark, A. R., & Smye, A. J. (2020). Active crustal differentiation beneath the Rio Grande Rift. *Nature Geoscience*, *13*(11), 758–763. https://doi.org/10.1038/s41561-020-0640-z

Clemens, J. (1990). *The granulite—granite connexion, Granulites and crustal evolution* (pp. 25–36). Springer.

Clemens, J. D. (2006). *Melting of the continental crust: Fluid regimes, melting reactions, and source-rock fertility*. Cambridge University Press.

Crisp, L. J., Berry, A. J., Burnham, A. D., Miller, L. A., & Newville, M. (2023). The Ti-in-zircon thermometer revised: The effect of pressure on the Ti site in zircon. *Geochimica et Cosmochimica Acta*, *360*, 241–258. https://doi.org/10.1016/j.gca.2023.04.031

Currie, C. A., & Hyndman, R. D. (2006). The thermal structure of subduction zone back arcs. *Journal of Geophysical Research*, *111*(B8). https://doi.org/10.1029/2005jb004024

Del Pilar-Martínez, A., Samaniego, A. F. N., Moreno, E. A., Arias, A. M. S., Moya, M. J. P. O., Álvarez, S. A. A., & Levresse, G. (2021). *Digital geological map and geochronological database of the Cenozoic cover of the southern Mesa Central province, Mexico* (pp. 1–10). Terra Digitalis.

Dickinson, W. R. (2006). Geotectonic evolution of the Great Basin. *Geosphere*, *2*(7), 353–368. https://doi.org/10.1130/ges00054.1

Dickinson, W. R., & Gehrels, G. E. (2003). U–Pb ages of detrital zircons from Permian and Jurassic eolian sandstones of the Colorado Plateau, USA: Paleogeographic implications. *Sedimentary Geology*, *163*(1–2), 29–66. https://doi.org/10.1016/s0037-0738(03)00158-1

Droop, G. T. R. (1987). A general equation for estimating Fe3+ concentrations in ferromagnesian silicates and oxides from microprobe analyses, using stoichiometric criteria. *Mineralogical Magazine*, *51*(361), 431–435. https://doi.org/10.1180/minmag.1987.051.361.10

Droubi, O. K., Bauer, A. M., Bonamici, C., Nachlas, W. O., Tappa, M. J., Garber, J. M., & Reimink, J. R. (2023). U-Th-Pb and trace element evaluation of existing titanite and apatite LA-ICP-MS reference materials and determination of 208Pb/232Th-206Pb/238U date discordance in Archaean accessory phases. *Geostandards and Geoanalytical Research*, *47*(2), 337–369. https://doi.org/10.1111/ggr.12488

Droubi, O. K., Cipar, J. H., Smye, A. J., & Garber, J. M. (2024). Xenolith petrochronology (San Luis Potosi, Mexico) constrains heat sources for Cenozoic ultrahigh-temperature metamorphism in the lower crust [Dataset and Software]. *Open Science Framework*. https://doi.org/10.17605/OSF.IO/543QS

Dumond, G., Williams, M. L., & Regan, S. P. (2018). The Athabasca granulite terrane and evidence for dynamic behavior of lower continental crust. *Annual Review of Earth and Planetary Sciences*, *46*(1), 353–386. https://doi.org/10.1146/annurev-earth-063016-020625

English, J. M., & Johnston, S. T. (2004). The Laramide orogeny: What were the driving forces? *International Geology Review*, *46*(9), 833–838. https://doi.org/10.2747/0020-6814.46.9.833

Ewing, T. A., Hermann, J., & Rubatto, D. (2013). The robustness of the Zr-in-rutile and Ti-in-zircon thermometers during high-temperature metamorphism (Ivrea-Verbano Zone, northern Italy). *Contributions to Mineralogy and Petrology*, *165*(4), 757–779. https://doi.org/10.1007/s00410-012-0834-5

Ferrari, L., Orozco-Esquivel, T., Bryan, S. E., Lopez-Martinez, M., & Silva-Fragoso, A. (2018). Cenozoic magmatism and extension in western Mexico: Linking the Sierra Madre Occidental silicic large igneous province and the Comondú Group with the Gulf of California rift. *Earth-Science Reviews*, *183*, 115–152. https://doi.org/10.1016/j.earscirev.2017.04.006

Ferrari, L., Orozco-Esquivel, T., Manea, V., & Manea, M. (2012). The dynamic history of the Trans-Mexican Volcanic Belt and the Mexico subduction zone. *Tectonophysics*, *522*, 122–149. https://doi.org/10.1016/j.tecto.2011.09.018

Ferry, J. M., & Watson, E. B. (2007). New thermodynamic models and revised calibrations for the Ti-in-zircon and Zr-in-rutile thermometers. *Contributions to Mineralogy and Petrology*, *154*(4), 429–437. https://doi.org/10.1007/s00410-007-0201-0

Fitz-Díaz, E., Lawton, T. F., Juárez-Arriaga, E., & Chávez-Cabello, G. (2018). The Cretaceous-Paleogene Mexican orogen: Structure, basin development, magmatism and tectonics. *Earth-Science Reviews*, *183*, 56–84. https://doi.org/10.1016/j.earscirev.2017.03.002

Frost, B. R., & Chacko, T. (1989). The granulite uncertainty principle: Limitations on thermobarometry in granulites. *The Journal of Geology*, *97*(4), 435–450. https://doi.org/10.1086/629321

Fu, B., Page, F., Cavosie, A. J., Fournelle, J., Kita, N. T., Lackey, J. S., et al. (2008). Ti-in-zircon thermometry: Applications and limitations. *Contributions to Mineralogy and Petrology*, *156*(2), 197–215. https://doi.org/10.1007/s00410-008-0281-5

Garber, J. M., Hacker, B. R., Kylander-Clark, A. R. C., Stearns, M., & Seward, G. (2017). Controls on trace element uptake in metamorphic titanite: Implications for petrochronology. *Journal of Petrology*, *58*(6), 1031–1057. https://doi.org/10.1093/petrology/egx046

George, F. R., Gaidies, F., & Boucher, B. (2018). Population-wide garnet growth zoning revealed by LA-ICP-MS mapping: Implications for trace element equilibration and syn-kinematic deformation during crystallisation. *Contributions to Mineralogy and Petrology*, *173*(9), 1–22. https://doi.org/10.1007/s00410-018-1503-0

Hacker, B. R., Kelemen, P. B., & Behn, M. D. (2015). Continental lower crust. *Annual Review of Earth and Planetary Sciences*, *43*(1), 167–205. https://doi.org/10.1146/annurev-earth-050212-124117

Harley, S. (1989). The origins of granulites: A metamorphic perspective. *Geological Magazine*, *126*(3), 215–247. https://doi.org/10.1017/S0016756800022330

Harley, S. L. (1990). High-temperature granulites. *Nature*, *347*(6289), 132–133. https://doi.org/10.1038/347132b0

Harte, B., & Barnicoat, A. (1990). High-temperature granulites. *Nature*, *347*(6289), 133. https://doi.org/10.1038/347133a0

Hayob, J. L., Essene, E. J., & Ruiz, J. (1990). High-temperature granulites. *Nature*, *347*(6289), 133–134. https://doi.org/10.1038/347133a0

Hayob, J. L., Essene, E. J., Ruiz, J., Ortega-Gutiérrez, F., & Aranda-Gómez, J. J. (1989). Young high-temperature granulites from the base of the crust in central Mexico. *Nature*, *342*(6247), 265–268. https://doi.org/10.1038/342265a0

Henry, C. D., & Aranda-Gomez, J. J. (1992). The real southern Basin and Range: Mid-to late Cenozoic extension in Mexico. *Geology*, *20*(8), 701–704. https://doi.org/10.1130/0091-7613(1992)020<0701:trsbar>2.3.co;2

Hermann, J., & Rubatto, D. (2009). Accessory phase control on the trace element signature of sediment melts in subduction zones. *Chemical Geology*, *265*(3–4), 512–526. https://doi.org/10.1016/j.chemgeo.2009.05.018

Herzberg, C. T., Fyfe, W. S., & Carr, M. J. (1983). Density constraints on the formation of the continental Moho and crust. *Contributions to Mineralogy and Petrology*, *84*, 1–5. https://doi.org/10.1007/bf01132324

Hesse, M. A. (2012). A finite volume method for trace element diffusion and partitioning during crystal growth. *Computers & Geosciences*, *46*, 96–106. https://doi.org/10.1016/j.cageo.2012.04.009

Hiess, J., Condon, D. J., McLean, N., & Noble, S. R. (2012). 238U/235U systematics in terrestrial uranium-bearing minerals. *Science*, *335*(6076), 1610–1614. https://doi.org/10.1126/science.1215507

Hirsch, D. M., Prior, D. J., & Carlson, W. D. (2003). An overgrowth model to explain multiple, dispersed high-Mn regions in the cores of garnet porphyroblasts. *American Mineralogist*, *88*(1), 131–141. https://doi.org/10.2138/am-2003-0116

Hokada, T., & Harley, S. L. (2004). Zircon growth in UHT leucosome: Constraints from zircon-garnet rare earth elements (REE) relations in Napier Complex, East Antarctica. *Journal of Mineralogical and Petrological Sciences*, *99*(4), 180–190. https://doi.org/10.2465/jmps.99.180

Holder, R. M., Yakymchuk, C., & Viete, D. R. (2020). Accessory mineral Eu anomalies in suprasolidus rocks: Beyond feldspar. *Geochemistry, Geophysics, Geosystems*, *21*(8), e2020GC009052. https://doi.org/10.1029/2020gc009052

Holland, T. J. B., Green, E. C. R., & Powell, R. (2022). A thermodynamic model for feldspars in KAlSi3O8– NaAlSi3O8– CaAl2Si2O8 for mineral equilibrium calculations. *Journal of Metamorphic Geology*, *40*(4), 587–600. https://doi.org/10.1111/jmg.12639

Holland, T. J. B., & Powell, R. (2011). An improved and extended internally consistent thermodynamic dataset for phases of petrological interest, involving a new equation of state for solids. *Journal of Metamorphic Geology*, *29*(3), 333–383. https://doi.org/10.1111/j.1525-1314.2010.00923.x

Hollister, L. S. (1966). Garnet zoning: An interpretation based on the Rayleigh fractionation model. *Science*, *154*(3757), 1647–1651. https://doi.org/10.1126/science.154.3757.1647

Holycross, M. E., & Bruce Watson, E. (2016). Diffusive fractionation of trace elements in basaltic melt. *Contributions to Mineralogy and Petrology*, *171*(10), 1–15. https://doi.org/10.1007/s00410-016-1289-x

Holycross, M. E., & Watson, E. B. (2018). Trace element diffusion and kinetic fractionation in wet rhyolitic melt. *Geochimica et Cosmochimica Acta*, *232*, 14–29. https://doi.org/10.1016/j.gca.2018.04.006

Housh, T. B., Aranda-Gómez, J. J., & Luhr, J. F. (2010). Isla Isabel (Nayarit, México): Quaternary alkalic basalts with mantle xenoliths erupted in the mouth of the Gulf of California. *Journal of Volcanology and Geothermal Research*, *197*(1–4), 85–107. https://doi.org/10.1016/j.jvolgeores.2009.06.011

Hyndman, R. D. (2017). Lower-crustal flow and detachment in the North American Cordillera: A consequence of Cordillera-wide high temperatures. *Geophysical Journal International*, *209*(3), 1779–1799. https://doi.org/10.1093/gji/ggx138

Iwamori, H., Yoshida, K., Nakamura, H., Kuwatani, T., Hamada, M., Haraguchi, S., & Ueki, K. (2017). Classification of geochemical data based on multivariate statistical analyses: Complementary roles of cluster, principal component, and independent component analyses. *Geochemistry, Geophysics, Geosystems*, *18*(3), 994–1012. https://doi.org/10.1002/2016gc006663

Jackson, S. E., Pearson, N. J., Griffin, W. L., & Belousova, E. A. (2004). The application of laser ablation-inductively coupled plasma-mass spectrometry to in situ U–Pb zircon geochronology. *Chemical Geology*, *211*(1–2), 47–69. https://doi.org/10.1016/j.chemgeo.2004.06.017

Jaffey, A. H., Flynn, K. F., Glendenin, L. E., Bentley, W. T., & Essling, A. M. (1971). Precision measurement of half-lives and specific activities of 235U and 238U. *Physical Review C*, *4*(5), 1889–1906. https://doi.org/10.1103/physrevc.4.1889

Jamieson, R. A., Beaumont, C., Medvedev, S., & Nguyen, M. H. (2004). Crustal channel flows: 2. Numerical models with implications for metamorphism in the Himalayan-Tibetan orogen. *Journal of Geophysical Research*, *109*(B6). https://doi.org/10.1029/2003jb002811

Jiao, S., Brown, M., Mitchell, R. N., Chowdhury, P., Clark, C., Chen, L., et al. (2023). Mechanisms to generate ultrahigh-temperature metamorphism. *Nature Reviews Earth & Environment*, *4*(5), 298–318. https://doi.org/10.1038/s43017-023-00403-2

Jochum, K. P., Stoll, B., Herwig, K., Willbold, M., Hofmann, A. W., Amini, M., et al. (2006). MPI-DING reference glasses for in situ microanalysis: New reference values for element concentrations and isotope ratios. *Geochemistry, Geophysics, Geosystems*, *7*(2). https://doi.org/10.1029/2005gc001060

Jollands, M. C., Bloch, E., & Müntener, O. (2020). New Ti-in-quartz diffusivities reconcile natural Ti zoning with time scales and temperatures of upper crustal magma reservoirs. *Geology*, *48*(7), 654–657. https://doi.org/10.1130/g47238.1

Kirkland, C. L., Smithies, R. H., Taylor, R. J. M., Evans, N., & McDonald, B. (2015). Zircon Th/U ratios in magmatic environs. *Lithos*, *212*, 397–414. https://doi.org/10.1016/j.lithos.2014.11.021

Kohn, M. J. (2009). Models of garnet differential geochronology. *Geochimica et Cosmochimica Acta*, *73*(1), 170–182. https://doi.org/10.1016/j.gca.2008.10.004

Konrad-Schmolke, M., Halama, R., Chew, D., Heuzé, C., De Hoog, J., & Ditterova, H. (2022). Discrimination of thermodynamic and kinetic contributions to the heavy rare earth element patterns in metamorphic garnet. *Journal of Metamorphic Geology*, *41*(4), 465–490. https://doi.org/10.1111/jmg.12703

Konrad-Schmolke, M., O'Brien, P. J., de Capitani, C., & Carswell, D. A. (2008). Garnet growth at high-and ultra-high pressure conditions and the effect of element fractionation on mineral modes and composition. *Lithos*, *103*(3–4), 309–332. https://doi.org/10.1016/j.lithos.2007.10.007

Laurent, O., Couzinié, S., & Doucet, L. S. (2023). Timescales of ultra-high temperature metamorphism and crustal differentiation: Zircon petrochronology from granulite xenoliths of the Variscan French Massif Central. *Earth and Planetary Science Letters*, *611*, 118133. https://doi.org/10.1016/j.epsl.2023.118133

Liu, S. J., Li, J. H., & Santosh, M. (2010). First application of the revised Ti-in-zircon geothermometer to Paleoproterozoic ultrahigh-temperature granulites of Tuguiwula, Inner Mongolia, North China Craton. *Contributions to Mineralogy and Petrology*, *159*(2), 225–235. https://doi.org/10.1007/s00410-009-0425-2

Liu, Y., Hu, Z., Gao, S., Günther, D., Xu, J., Gao, C., & Chen, H. (2008). In situ analysis of major and trace elements of anhydrous minerals by LA-ICP-MS without applying an internal standard. *Chemical Geology*, *257*(1–2), 34–43. https://doi.org/10.1016/j.chemgeo.2008.08.004

Longerich, H. P., Jackson, S. E., & Gunther, D. (1996). Inter-laboratory note. Laser ablation inductively coupled plasma-mass spectrometric transient signal data acquisition and analyte concentration calculation. *Journal of Analytical Atomic Spectrometry*, *11*(9), 899–904. https://doi.org/10.1039/ja9961100899

Luhr, J. F., & Aranda-Gómez, J. J. (1997). Mexican peridotite xenoliths and tectonic terranes: Correlations among vent location, texture, temperature, pressure, and oxygen fugacity. *Journal of Petrology*, *38*(8), 1075–1112. https://doi.org/10.1093/petrology/38.8.1075

Luhr, J. F., Aranda-Gomez, J. J., & Pier, J. G. (1989). Spinel-lherzolite-bearing quaternary volcanic centers in San Luis Potosí, Mexico: 1. Geology, mineralology, and petrology. *Journal of Geophysical Research*, *94*(B6), 7916–7940. https://doi.org/10.1029/jb094ib06p07916

Luhr, J. F., Pier, J. G., Aranda-Gómez, J. J., & Podosek, F. A. (1995). Crustal contamination in early Basin-and-Range hawaiites of the Los Encinos volcanic field, central México. *Contributions to Mineralogy and Petrology*, *118*(4), 321–339. https://doi.org/10.1007/s004100050018

Martini, M., Ferrari, L., López-Martínez, M., Cerca-Martínez, M., Valencia, V., Serrano-Durán, L., et al. (2009). Cretaceous–Eocene magmatism and Laramide deformation in southwestern Mexico: No role for terrane accretion. In *Backbone of the Americas: Shallow subduction, plateau uplift, and ridge and terrane collision: Geological Society of America Memoir* (Vol. 204, pp. 151–182).

Martini, M., & Ortega-Gutiérrez, F. (2018). Tectono-stratigraphic evolution of eastern Mexico during the break-up of Pangea: A review. *Earth-Science Reviews*, *183*, 38–55. https://doi.org/10.1016/j.earscirev.2016.06.013

McDowell, F. W., Clabaugh, S. E., Chapin, C. E., & Elston, W. E. (1979). Ignimbrites of the Sierra Madre Occidental and their relation to the tectonic history of western Mexico (Vol. *180*, pp. 113–124). *Geological Society of America Special Paper*. https://doi.org/10.1130/spe180-p113

Mckenzie, D., & Bickle, M. J. (1988). The volume and composition of melt generated by extension of the lithosphere. *Journal of Petrology*, *29*(3), 625–679. https://doi.org/10.1093/petrology/29.3.625

Meyer, M., John, T., Brandt, S., & Klemd, R. (2011). Trace element composition of rutile and the application of Zr-in-rutile thermometry to UHT metamorphism (Epupa Complex, NW Namibia). *Lithos*, *126*(3–4), 388–401. https://doi.org/10.1016/j.lithos.2011.07.013

Mitchell, R. J., & Harley, S. L. (2017). Zr-in-rutile resetting in aluminosilicate bearing ultra-high temperature granulites: Refining the record of cooling and hydration in the Napier Complex, Antarctica. *Lithos*, *272*, 128–146. https://doi.org/10.1016/j.lithos.2016.11.027

Nabelek, P. I., Whittington, A. G., & Hofmeister, A. M. (2010). Strain heating as a mechanism for partial melting and ultrahigh temperature metamorphism in convergent orogens: Implications of temperature-dependent thermal diffusivity and rheology. *Journal of Geophysical Research*, *115*(B12). https://doi.org/10.1029/2010jb007727

Nieto-Samaniego, A. F., Alaniz-Álvarez, S. A., & Camprubí, A. (2007). Mesa Central of México: Stratigraphy, structure, and Cenozoic tectonic evolution. In S. A. Alaniz-Álvarez & Á. F. Nieto-Samaniego (Eds.), *Geology of México: Celebrating the centenary of the geological society of México* (Vol. 422, pp. 41–70). Geological Society of America Special Paper.

Ogier, E. (2023). EEP. MATLAB Central File Exchange. https://www.mathworks.com/matlabcentral/fileexchange/56317-eep

Osborne, Z. R., Thomas, J. B., Nachlas, W. O., Angel, R. J., Hoff, C. M., & Watson, E. B. (2022). TitaniQ revisited: Expanded and improved Ti-in-quartz solubility model for thermobarometry. *Contributions to Mineralogy and Petrology*, *177*(3), 31. https://doi.org/10.1007/s00410-022-01896-8

Otamendi, J. E., de La Rosa, J. D., Douce, A. E. P., & Castro, A. (2002). Rayleigh fractionation of heavy rare earths and yttrium during metamorphic garnet growth. *Geology*, *30*(2), 159–162. https://doi.org/10.1130/0091-7613(2002)030<0159:rfohre>2.0.co;2

Paton, C., Hellstrom, J., Paul, B., Woodhead, J., & Hergt, J. (2011). Iolite: Freeware for the visualisation and processing of mass spectrometric data. *Journal of Analytical Atomic Spectrometry*, *26*(12), 2508–2518. https://doi.org/10.1039/c1ja10172b

Paton, C., Woodhead, J. D., Hellstrom, J. C., Hergt, J. M., Greig, A., & Maas, R. (2010). Improved laser ablation U-Pb zircon geochronology through robust downhole fractionation correction. *Geochemistry, Geophysics, Geosystems*, *11*(3). https://doi.org/10.1029/2009gc002618

Pearce, N. J., Perkins, W. T., Westgate, J. A., Gorton, M. P., Jackson, S. E., Neal, C. R., & Chenery, S. P. (1997). A compilation of new and published major and trace element data for NIST SRM 610 and NIST SRM 612 glass reference materials. *Geostandards Newsletter: The Journal of Geostandards and Geoanalysis*, *21*(1), 115–144. https://doi.org/10.1111/j.1751-908x.1997.tb00538.x

Pedregosa, F., Varoquaux, G., Gramfort, A., Michel, V., Thirion, B., Grisel, O., et al. (2011). Scikit-learn: Machine learning in Python. *Journal of Machine Learning Research*, *12*, 2825–2830.

Peredo, C. R., Yutsis, V., Martin, A. J., & Aranda-Gómez, J. J. (2021). Crustal structure and Curie point depth in central Mexico inferred from the spectral analysis and forward modeling of potential field data. *Journal of South American Earth Sciences*, *112*, 103565. https://doi.org/10.1016/j.jsames.2021.103565

Piazolo, S., Belousova, E., La Fontaine, A., Corcoran, C., & Cairney, J. M. (2017). Trace element homogeneity from micron-to atomic scale: Implication for the suitability of the zircon GJ-1 as a trace element reference material. *Chemical Geology*, *456*, 10–18. https://doi.org/10.1016/j.chemgeo.2017.03.001

Platt, J. P., & England, P. C. (1994). Convective removal of lithosphere beneath mountain belts; thermal and mechanical consequences. *American Journal of Science*, *294*(3), 307–336. https://doi.org/10.2475/ajs.294.3.307

Pool, G. B. (1990). *Petrology, geochemistry and geochronology of lower-crustal xenoliths, central Mexico* (Doctoral dissertation). Washington University.

Raisz, E. (1964). *Landforms of México* (2nd ed.). Prepared for the geography branch of the office of naval research.

Raye, U., Anthony, E. Y., Stern, R. J., Kimura, J. I., Ren, M., Qing, C., & Tani, K. (2011). Composition of the mantle lithosphere beneath south-central Laurentia: Evidence from peridotite xenoliths, Knippa, Texas. *Geosphere*, *7*(3), 710–723. https://doi.org/10.1130/ges00618.1

Reid, M. R. (1990). Ionprobe investigation of rare earth element distributions and partial melting of metasedimentary granulites. In *Granulites and crustal evolution* (pp. 507–522).

Reid, M. R., Hart, S. R., Padovani, E. R., & Wandless, G. A. (1989). Contribution of metapelitic sediments to the composition, heat production, and seismic velocity of the lower crust of southern New Mexico, USA. *Earth and Planetary Science Letters*, *95*(3–4), 367–381. https://doi.org/10.1016/0012-821x(89)90111-8

Ringwood, M. F., Rudnick, R. L., & Kylander-Clark, A. R. (2023). Metasediments from the lower crust reveal the history of the Picuris orogeny, southwest USA. *Geological Society of America Bulletin*. https://doi.org/10.1130/b36836.1

Rubatto, D. (2002). Zircon trace element geochemistry: Partitioning with garnet and the link between U–Pb ages and metamorphism. *Chemical Geology*, *184*(1–2), 123–138. https://doi.org/10.1016/s0009-2541(01)00355-2

Rubatto, D., Burger, M., Lanari, P., Hattendorf, B., Schwarz, G., Neff, C., et al. (2020). Identification of growth mechanisms in metamorphic garnet by high-resolution trace element mapping with LA-ICP-TOFMS. *Contributions to Mineralogy and Petrology*, *175*(7), 61. https://doi.org/10.1007/s00410-020-01700-5

Rubatto, D., & Hermann, J. (2007). Experimental zircon/melt and zircon/garnet trace element partitioning and implications for the geochronology of crustal rocks. *Chemical Geology*, *241*(1–2), 38–61. https://doi.org/10.1016/j.chemgeo.2007.01.027

Rudnick, R. L., & Cameron, K. L. (1991). Age diversity of the deep crust in northern Mexico. *Geology*, *19*(12), 1197–1200. https://doi.org/10.1130/0091-7613(1991)019<1197:adotdc>2.3.co;2

Rudnick, R. L., & Gao, S. (2003). Composition of the continental crust. *The Crust*, *3*, 1–64. https://doi.org/10.1016/b0-08-043751-6/03016-4

Ruiz, J., Patchett, P. J., & Arculus, R. J. (1988). Nd-Sr isotope composition of lower crustal xenoliths—Evidence for the origin of mid-Tertiary felsic volcanics in Mexico. *Contributions to Mineralogy and Petrology*, *99*(1), 36–43. https://doi.org/10.1007/bf00399363

Sammon, L. G., & McDonough, W. F. (2021). A geochemical review of amphibolite, granulite, and eclogite facies lithologies: Perspectives on the deep continental crust. *Journal of Geophysical Research: Solid Earth*, *126*(12), e2021JB022791. https://doi.org/10.1029/2021jb022791

Sandiford, M., & Powell, R. (1990). Some isostatic and thermal consequences of the vertical strain geometry in convergent orogens. *Earth and Planetary Science Letters*, *98*(2), 154–165. https://doi.org/10.1016/0012-821x(90)90056-4

Sawyer, E. W., Cesare, B., & Brown, M. (2011). When the continental crust melts. *Elements*, *7*(4), 229–234. https://doi.org/10.2113/gselements.7.4.229

Schaaf, P., Heinrich, W., & Besch, T. (1994). Composition and Sm-Nd isotopic data of the lower crust beneath San Luis Potosí, central Mexico: Evidence from a granulite-facies xenolith suite. *Chemical Geology*, *118*(1–4), 63–84. https://doi.org/10.1016/0009-2541(94)90170-8

Scherer, E. E. (1999). *Lutetium-hafnium geochronology and the ages of lower crustal xenoliths from Kilbourne Hole, New Mexico*. University of California.

Scherer, E. E., Cameron, K. L., Johnson, C. M., Beard, B. L., Barovich, K. M., & Collerson, K. D. (1997). Lu-Hf geochronology applied to dating Cenozoic events affecting lower crustal xenoliths from Kilbourne Hole, New Mexico. *Chemical Geology*, *142*(1–2), 63–78. https://doi.org/10.1016/s0009-2541(97)00076-4

Schorn, S., Diener, J. F., Powell, R., & Stüwe, K. (2018). Thermal buffering in the orogenic crust. *Geology*, *46*(7), 643–646. https://doi.org/10.1130/g40246.1

Sedlock, R. L., Ortega-Gutiérrez, F., & Speed, R. C. (1993). Tectonostratigraphic terranes and tectonic evolution of Mexico.

Silva-Romo, G., Arellano-Gil, J., Mendoza-Rosales, C., & Nieto-Obregón, J. (2000). A submarine fan in the Mesa Central, Mexico. *Journal of South American Earth Sciences*, *13*(4–5), 429–442. https://doi.org/10.1016/s0895-9811(00)00034-1

Skora, S., Baumgartner, L. P., Mahlen, N. J., Johnson, C. M., Pilet, S., & Hellebrand, E. (2006). Diffusion-limited REE uptake by eclogite garnets and its consequences for Lu–Hf and Sm–Nd geochronology. *Contributions to Mineralogy and Petrology*, *152*(6), 703–720. https://doi.org/10.1007/s00410-006-0128-x

Sláma, J., Košler, J., Condon, D. J., Crowley, J. L., Gerdes, A., Hanchar, J. M., et al. (2008). Plešovice zircon—A new natural reference material for U–Pb and Hf isotopic microanalysis. *Chemical Geology*, *249*(1–2), 1–35. https://doi.org/10.1016/j.chemgeo.2007.11.005

Solari, L. A., Aranda-Gómez, J. J., Moreno-Arredondo, A., & Maldonado, R. (2023). U-Pb age of a late Cenozoic ultra-high temperature metamorphic event under Central Mexico, as inferred from granulite xenoliths from Cerro El Toro, Mexico. *International Geology Review*, *65*(3), 335–356. https://doi.org/10.1080/00206814.2022.2045640

Spear, F. S., & Kohn, M. J. (1996). Trace element zoning in garnet as a monitor of crustal melting. *Geology*, *24*(12), 1099–1102. https://doi.org/10.1130/0091-7613(1996)024<1099:teziga>2.3.co;2

Stacey, J. S., & Kramers, J. D. (1975). Approximation of terrestrial lead isotope evolution by a two-stage model. *Earth and Planetary Science Letters*, *26*(2), 207–221. https://doi.org/10.1016/0012-821x(75)90088-6

Štípská, P., Powell, R., Hacker, B. R., Holder, R., & Kylander-Clark, A. R. C. (2016). Uncoupled U/Pb and REE response in zircon during the transformation of eclogite to mafic and intermediate granulite (Blanský les, Bohemian Massif). *Journal of Metamorphic Geology*, *34*(6), 551–572. https://doi.org/10.1111/jmg.12193

Stull, R. J., & McMILLAN, K. (1973). Origin of Lherzolite inclusions in the Malapai Hill Basalt, Joshua Tree National Monument, California. *Geological Society of America Bulletin*, *84*(7), 2343–2350. https://doi.org/10.1130/0016-7606(1973)84<2343:ooliit>2.0.co;2

Taylor, R. J. M., Clark, C., Harley, S. L., Kylander-Clark, A. R. C., Hacker, B. R., & Kinny, P. D. (2017). Interpreting granulite facies events through rare earth element partitioning arrays. *Journal of Metamorphic Geology*, *35*(7), 759–775. https://doi.org/10.1111/jmg.12254

Taylor, R. J. M., Harley, S. L., Hinton, R. W., Elphick, S., Clark, C., & Kelly, N. M. (2015). Experimental determination of REE partition coefficients between zircon, garnet and melt: A key to understanding high-T crustal processes. *Journal of Metamorphic Geology*, *33*(3), 231–248. https://doi.org/10.1111/jmg.12118

Thomas, J. B., Bruce Watson, E., Spear, F. S., Shemella, P. T., Nayak, S. K., & Lanzirotti, A. (2010). TitaniQ under pressure: The effect of pressure and temperature on the solubility of Ti in quartz. *Contributions to Mineralogy and Petrology*, *160*(5), 743–759. https://doi.org/10.1007/s00410-010-0505-3

Tomkins, H. S., Powell, R., & Ellis, D. J. (2007). The pressure dependence of the zirconium-in-rutile thermometer. *Journal of Metamorphic Geology*, *25*(6), 703–713. https://doi.org/10.1111/j.1525-1314.2007.00724.x

Tristán-González, M., Aguirre-Díaz, G. J., Labarthe-Hernández, G., Torres-Hernández, J. R., & Bellon, H. (2009). Post-Laramide and pre-Basin and Range deformation and implications for Paleogene (55–25 Ma) volcanism in central Mexico: A geological basis for a volcano-tectonic stress model. *Tectonophysics*, *471*(1–2), 136–152. https://doi.org/10.1016/j.tecto.2008.12.021

Van Orman, J. A., Grove, T. L., Shimizu, N., & Layne, G. D. (2002). Rare earth element diffusion in a natural pyrope single crystal at 2.8 GPa. *Contributions to Mineralogy and Petrology*, *142*(4), 416–424. https://doi.org/10.1007/s004100100304

Vermeesch, P. (2018). IsoplotR: A free and open toolbox for geochronology. *Geoscience Frontiers*, *9*(5), 1479–1493. https://doi.org/10.1016/j.gsf.2018.04.001

Vielzeuf, D., Clemens, J. D., Pin, C., & Moinet, E. (1990). Granites, granulites, and crustal differentiation. In *Granulites and crustal evolution* (pp. 59–85).

Vielzeuf, D., & Holloway, J. R. (1988). Experimental determination of the fluid-absent melting relations in the pelitic system: Consequences for crustal differentiation. *Contributions to Mineralogy and Petrology*, *98*(3), 257–276. https://doi.org/10.1007/bf00375178

Warr, L. (2021). IMA–CNMNC approved mineral symbols. *Mineralogical Magazine*, *85*(3), 291–320. https://doi.org/10.1180/mgm.2021.43

Warren, R. G., Kudo, A. M., & Keil, K. (1979). Geochemistry of lithic and single-crystal inclusions in basalt and a characterization of the upper mantle-lower crust in the Engle Basin, Rio Grande Rift, New Mexico. Rio Grande Rift: Tectonics and magmatism, *14*, 393–415.

Wetherill, G. W. (1956). Discordant uranium-lead ages, I. *Eos, Transactions American Geophysical Union*, *37*(3), 320–326. https://doi.org/10.1029/TR037i003p00320

White, R. W., & Powell, R. (2002). Melt loss and the preservation of granulite facies mineral assemblages. *Journal of Metamorphic Geology*, *20*(7), 621–632. https://doi.org/10.1046/j.1525-1314.2002.00206_20_7.x

White, R. W., Powell, R., Holland, T. J. B., Johnson, T. E., & Green, E. C. R. (2014b). New mineral activity–composition relations for thermodynamic calculations in metapelitic systems. *Journal of Metamorphic Geology*, *32*(3), 261–286. https://doi.org/10.1111/jmg.12071

White, R. W., Powell, R., & Johnson, T. E. (2014a). The effect of Mn on mineral stability in metapelites revisited: New a–x relations for manganese-bearing minerals. *Journal of Metamorphic Geology*, *32*(8), 809–828. https://doi.org/10.1111/jmg.12095

Whitehouse, M. J., & Platt, J. P. (2003). Dating high-grade metamorphism—Constraints from rare-earth elements in zircon and garnet. *Contributions to Mineralogy and Petrology*, *145*(1), 61–74. https://doi.org/10.1007/s00410-002-0432-z

Whittington, A. G., Hofmeister, A. M., & Nabelek, P. I. (2009). Temperature-dependent thermal diffusivity of the Earth's crust and implications for magmatism. *Nature*, *458*(7236), 319–321. https://doi.org/10.1038/nature07818

Wiedenbeck, M., Hanchar, J. M., Peck, W. H., Sylvester, P., Valley, J., Whitehouse, M., et al. (2004). Further characterisation of the 91500 zircon crystal. *Geostandards and Geoanalytical Research*, *28*(1), 9–39. https://doi.org/10.1111/j.1751-908x.2004.tb01041.x

Williams, M. A., Kelsey, D. E., & Rubatto, D. (2022). Thorium zoning in monazite: A case study from the Ivrea–Verbano zone, NW Italy. *Journal of Metamorphic Geology*, *40*(6), 1015–1042. https://doi.org/10.1111/jmg.12656

Wilshire, H. G., Meyer, C. E., Nakata, J. K., Calk, L. C., Shervais, J. W., Nielson, J. E., & Schwarzman, E. C. (1988). *Mafic and ultramafic xenoliths from volcanic rocks of the western United States* (Vol. 1443). US Government Printing Office.

Wu, L. G., Li, Y., Jollands, M. C., Vermeesch, P., & Li, X. H. (2022). Diffuser: A user-friendly program for diffusion chronometry with robust uncertainty estimation. *Computers & Geosciences*, *163*, 105108. https://doi.org/10.1016/j.cageo.2022.105108

Wyatt, D. C., Smye, A. J., Garber, J. M., & Hacker, B. R. (2022). Assembly and Tectonic Evolution of Continental Lower Crust: Monazite Petrochronology of the Ivrea-Verbano Zone (Val Strona di Omegna). *Tectonics*, *41*(3), e2021TC006841. https://doi.org/10.1029/2021tc006841

Yakymchuk, C., Kirkland, C. L., & Clark, C. (2018). Th/U ratios in metamorphic zircon. *Journal of Metamorphic Geology*, *36*(6), 715–737. https://doi.org/10.1111/jmg.12307